MDPI

Article

Multipole Moments Under Square Vortex and Skyrmion Crystals

Satoru Hayami

Graduate School of Science, Hokkaido University, Sapporo 060-0810, Japan; hayami@phys.sci.hokudai.ac.jp

Abstract: Non-coplanar spin textures such as magnetic vortices and skyrmions manifest themselves in unusual physical phenomena owing to their topologically nontrivial properties. Here, we investigate emergent multipole moments under vortex and skyrmion crystals in the centrosymmetric tetragonal system. Depending on the vorticity and helicity of the vortex or skyrmion, various multipole moments, including magnetic toroidal and electric toroidal multipoles, are induced on the atomic scale. In particular, the vortex and skyrmion spin textures consisting of multiple spin density waves give rise to density waves in terms of other multipole moments. Our results reveal a close relationship between non-coplanar multiple-Q spin textures and multipole moments.

Keywords: skyrmion; multipole; magnetic toroidal moment; electric toroidal moment; magnetic point group; density wave

1. Introduction

The interplay among internal electronic degrees of freedom such as charge, spin, and orbit has attracted much attention in condensed matter physics. For example, coupling between the charge and spin degrees of freedom leads to magnetoresistance [1–7], multiferroic properties [8–16], and the topological Hall/Nernst effect [17–28], whereas coupling between the spin and orbital degrees of freedom leads to the spin Hall effect [29–40], the Edelstein effect [41–49], and noncentrosymmetric superconductivity [50–56]. Thus, understanding the relationship between microscopic electronic degrees of freedom and macroscopic physical phenomena has been a central issue for years.

The concept of multipoles can connect such microscopic and macroscopic properties, as the symmetry-adapted basis consisting of multipoles, referred to as the symmetry-adapted multipole basis (SAMB), corresponds to a complete basis set in physical space [57,58]. The SAMB is constituted of four multipoles: the electric multipole, characterized by a time-reversal-even polar tensor; the magnetic multipole, characterized by a time-reversal-odd axial tensor; the magnetic toroidal multipole, characterized by a time-reversal-odd polar tensor; and the electric toroidal multipole, characterized by a time-reversal-even axial tensor. Reflecting its completeness, the SAMB can describe various order parameters under complicated electronic, magnetic, and lattice structures, such as chiral charge ordering with the electric toroidal monopole [59–61], ferroaxial ordering with the electric toroidal dipole [62–69], and non-coplanar magnetic ordering with the magnetic toroidal octupole [70]. Furthermore, emergent multipole moments can account for various physical properties, such as band-dispersion modulation, cross-correlation, and nonlinear transport from the microscopic viewpoint [71].

In the present study, we focus on the multipole moments induced by multiple-Q spin textures. A multiple-Q state is defined as a superposition of multiple spin density waves [72–77]. These states describe various topologically nontrivial spin textures, including vortex and skyrmion crystals [78–85]. Because these multiple-Q states often exhibit non-coplanar spin textures, various types of symmetry reduction are expected; hence, various multipole moments can be induced. To demonstrate this, we consider the double-Q vortex and skyrmion spin textures in the s–p orbital model on a two-dimensional square lattice, where the s–p orbital basis includes multiple monopolar, dipolar, quadrupolar,

and octupolar degrees of freedom in its Hilbert space. We show the multipole moments induced by the vortex and skyrmion spin textures with different vorticities and helicities. Our results provide rich multipole physics brought about by multiple-Q states.

The rest of this paper is organized as follows. In Section 2, we introduce a tight-binding model with s and p orbitals. We list all the multipole degrees of freedom in s-p orbital space. We also introduce the vortex and skyrmion spin textures consisting of a superposition of double-Q spiral waves. Then, we show the multipole moments induced under vortex and skyrmion crystals in Section 3, where both uniform and finite-q components of the multipole moments appear according to the type of vortex or skyrmion crystal. Finally, Section 4 concludes the paper.

2. Model

We start by introducing multipole moments. There are four types of multipoles, according to their spatial inversion ($\mathcal{P}$) and time-reversal ($\mathcal{T}$) parities: electric multipoles Q_{lm}, with $(\mathcal{P}, \mathcal{T}) = [(-1)^l, +1]$; magnetic multipoles M_{lm}, with $(\mathcal{P}, \mathcal{T}) = [(-1)^{l+1}, -1]$; magnetic toroidal multipoles T_{lm}, with $(\mathcal{P}, \mathcal{T}) = [(-1)^l, -1]$; and electric toroidal multipoles G_{lm}, with $(\mathcal{P}, \mathcal{T}) = [(-1)^{l+1}, +1]$, where l and m stand for the rank of the multipole and its component, respectively. Hereafter, we denote the monopole ($l = 0$) as X_0, the dipole ($l = 1$) as (X_x, X_y, X_z), the quadrupole ($l = 2$) as $(X_u, X_v, X_{yz}, X_{zx}, X_{xy})$, and the octupole ($l = 3$) as $(X_{xyz}, X_x^\alpha, X_y^\alpha, X_z^\alpha, X_x^\beta, X_y^\beta, X_z^\beta)$ for $X = Q, M, T, G$.

When we consider the four orbitals, consisting of one s orbital and three p orbitals, i.e., p_x, p_y, and p_z, the Hilbert space spanned by these four orbitals can be described by an 8×8 matrix with the spin degree of freedom; in other words, there are 64 independent matrix elements in the s–p hybridized system. By using the multipole operators defined in [86], the correspondence between the multipoles and matrix elements is obtained; see Appendix A for the specific expressions. In the spinless Hilbert space, the 16 active multipoles are as follows: the electric monopoles $Q_{s,0}$ and $Q_{p,0}$, electric dipoles $\boldsymbol{Q} = (Q_x, Q_y, Q_z)$, electric quadrupoles $(Q_u, Q_v, Q_{yz}, Q_{zx}, Q_{xy})$, magnetic dipoles $\boldsymbol{M} = (M_x, M_y, M_z)$, and magnetic toroidal dipoles $\boldsymbol{T} = (T_x, T_y, T_z)$. In the spinful Hilbert space, the other 48 multipoles with spin dependence are the electric monopole $Q_0^{(s)}$, the electric dipoles $(Q_x^{(s)}, Q_y^{(s)}, Q_z^{(s)})$, the electric quadrupoles $(Q_u^{(s)}, Q_v^{(s)}, Q_{yz}^{(s)}, Q_{zx}^{(s)}, Q_{xy}^{(s)})$, the magnetic monopole $M_0^{(s)}$, the magnetic dipoles $(M_{s,x}^{(s)}, M_{s,y}^{(s)}, M_{s,z}^{(s)})$, $(M_{p,x}^{(s)}, M_{p,y}^{(s)}, M_{p,z}^{(s)})$, and $(M_{a,x}^{(s)}, M_{a,y}^{(s)}, M_{a,z}^{(s)})$, the magnetic quadrupoles $(M_u^{(s)}, M_v^{(s)}, M_{yz}^{(s)}, M_{zx}^{(s)}, M_{xy}^{(s)})$, the magnetic octupoles $(M_{xyz}^{(s)}, M_x^{\alpha(s)}, M_y^{\alpha(s)}, M_z^{\alpha(s)}, M_x^{\beta(s)}, M_y^{\beta(s)}, M_z^{\beta(s)})$, the magnetic toroidal dipoles $(T_x^{(s)}, T_y^{(s)}, T_z^{(s)})$, the magnetic toroidal quadrupoles $(T_u^{(s)}, T_v^{(s)}, T_{yz}^{(s)}, T_{zx}^{(s)}, T_{xy}^{(s)})$, the electric toroidal monopole $G_0^{(s)}$, the electric toroidal dipoles $(G_x^{(s)}, G_y^{(s)}, G_z^{(s)})$, and the electric toroidal quadrupoles $(G_u^{(s)}, G_v^{(s)}, G_{yz}^{(s)}, G_{zx}^{(s)}, G_{xy}^{(s)})$, where the superscript (s) denotes a spin-dependent multipole. The active multipoles in the s–p hybridized orbital system are summarized in Table 1. It is noteworthy that similar multipoles are also active for different orbitals, such as the p–d and d–f orbitals; the following results for the s–p model can be straightforwardly applied to the other orbital cases, as the qualitative results are unaltered by of the choice of orbitals.

Table 1. Classification of multipole moments in the *s*–*p* hybridized orbital system: the upper panel shows the multipoles activated in spinless space, while the lower panel shows those activated in spinful space. Here, *l* means the rank of the multipole; see the main text for the details of the multipole notation.

- Without spin dependence			
basis	$l = 0$	$l = 1$	$l = 2$
s-s	$Q_{s,0}$		
p-p	$Q_{p,0}$	M_x, M_y, M_z	$Q_u, Q_v, Q_{yz}, Q_{zx}, Q_{xy}$
s-p		Q_x, Q_y, Q_z	
		T_x, T_y, T_z	

- With spin dependence			
basis	$l = 0$	$l = 1$	$l = 2$	$l = 3$
---	---	---	---	---
s-s		$M^{(s)}_{s,x}, M^{(s)}_{s,y}, M^{(s)}_{s,z}$		
p-p	$Q^{(s)}_0$	$M^{(s)}_{p,x}, M^{(s)}_{p,y}, M^{(s)}_{p,z}$	$Q^{(s)}_u, Q^{(s)}_v, Q^{(s)}_{yz}, Q^{(s)}_{zx}, Q^{(s)}_{xy}$	$M^{(s)}_{xyz}, M^{\alpha(s)}_x, M^{\alpha(s)}_y, M^{\alpha(s)}_z, M^{\beta(s)}_x, M^{\beta(s)}_y, M^{\beta(s)}_z$
		$M^{(s)}_{a,x}, M^{(s)}_{a,y}, M^{(s)}_{a,z}$	$T^{(s)}_u, T^{(s)}_v, T^{(s)}_{yz}, T^{(s)}_{zx}, T^{(s)}_{xy}$	
		$G^{(s)}_x, G^{(s)}_y, G^{(s)}_z$		
s-p	$G^{(s)}_0$	$Q^{(s)}_x, Q^{(s)}_y, Q^{(s)}_z$	$G^{(s)}_u, G^{(s)}_v, G^{(s)}_{yz}, G^{(s)}_{zx}, G^{(s)}_{xy}$	
	$M^{(s)}_0$	$T^{(s)}_x, T^{(s)}_y, T^{(s)}_z$	$M^{(s)}_u, M^{(s)}_v, M^{(s)}_{yz}, M^{(s)}_{zx}, M^{(s)}_{xy}$	

We consider a tight-binding model on a two-dimensional square lattice with spatial inversion symmetry under the D_{4h} symmetry, as there are no odd-parity multipoles or other unconventional multipole moments in the paramagnetic state, which enables us to investigate the relationship between multipole moments and magnetic structures. The Hamiltonian is provided by

$$\mathcal{H} = -\sum_{ij\alpha\alpha'\sigma}(t^{\alpha\alpha'}_{ij}c^{\dagger}_{i\alpha'\sigma}c_{j\alpha\sigma} + \text{H.c.}) + \frac{\lambda}{2}\sum_{i\tilde{\alpha}\tilde{\alpha}'\sigma\sigma'}c^{\dagger}_{i\tilde{\alpha}\sigma}H^{\text{SOC}}c_{i\tilde{\alpha}'\sigma'} + J\sum_{i\alpha\sigma\sigma'}c^{\dagger}_{i\alpha\sigma}\sigma_{\sigma\sigma'}c_{i\alpha\sigma'}\cdot\boldsymbol{M}'_i, \quad (1)$$

where $c^{\dagger}_{i\alpha\sigma}$ and $c_{i\alpha\sigma}$ represent the creation and annihilation Fermion operators at site *i*, orbital $\alpha = s$, p_x, p_y, and p_z (or $\tilde{\alpha} = p_x$, p_y, and p_z), and spin σ, respectively. The first term represents the kinetic energy of electrons, which includes nearest-neighbor hopping t_s between the *s* orbitals, hopping t_{xy} between the p_x and p_y orbitals, hopping t_z between the p_z orbitals, and hopping t_{sp} between the *s* and (p_x, p_y) orbitals, all of which are taken so as to preserve the symmetry of the tetragonal square-lattice structure. We ignore the orbital-dependent onsite potential for simplicity. The second term represents the atomic spin–orbit coupling for the *p* orbitals, where $\mathcal{H}^{\text{SOC}}$ is represented by the 6×6 matrix provided by

$$H^{\text{SOC}} = \begin{pmatrix} 0 & -i\sigma^z & i\sigma^y \\ i\sigma^z & 0 & -i\sigma^x \\ -i\sigma^y & i\sigma^x & 0 \end{pmatrix}, \quad (2)$$

where σ^{μ} is the $\mu = x, y, z$ component of the Pauli matrix in spin space. In the following calculations, we set $t_s = -1$, $t_{xy} = 0.7$, $t_z = 0.4$, $t_{sp} = 0.6$, and $\lambda = 0.5$, where t_s is set as the energy unit of the model.

The third term represents the effect of magnetic mean fields arising from the vortex and skyrmion spin textures; $J = 1$ is the coupling constant, and the orbital component is neglected for simplicity. We suppose that the effective site-dependent magnetic field $\boldsymbol{M}'_i$ is represented in the following forms. For the Néel-type vortex and skyrmion spin textures, $\boldsymbol{M}'_i$ is represented by

$$\boldsymbol{M}'_i = \mathcal{N}_i\begin{pmatrix} \cos\boldsymbol{Q}_1\cdot\boldsymbol{r}_i \\ \cos\boldsymbol{Q}_2\cdot\boldsymbol{r}_i \\ \tilde{M}_z - \sin\boldsymbol{Q}_1\cdot\boldsymbol{r}_i - \sin\boldsymbol{Q}_2\cdot\boldsymbol{r}_i \end{pmatrix}^{\text{T}}, \quad (3)$$

where the double-Q ordering wave vectors are provided by $\boldsymbol{Q}_1 = (\pi/3, 0)$ and $\boldsymbol{Q}_2 = (0, \pi/3)$; $\boldsymbol{r}_i$ is the position vector, $\mathcal{N}_i$ represents the local constraint to satisfy $|\boldsymbol{M}_i'| = 1$, and $\tilde{M}_z$ is the variational parameter corresponding to a net magnetization. For the vortex (skyrmion) crystal, $\tilde{M}_z = 0$ ($\tilde{M}_z = 0.5$) in the following calculations. The real-space spin configurations of the Néel-type vortex and skyrmion crystals are shown in Figure 1a and Figure 1b, respectively. In the vortex crystal in Figure 1a, the skyrmion number is zero owing to the cancellation of the spin scalar chirality between the cores with $M_z' = +1$ and $M_z' = -1$, where the vortex cores are located at the center of the square plaquette [87]. This state is also referred to as a meron–antimeron crystal. Meanwhile, the skyrmion number is -1 in the skyrmion crystal in Figure 1b.
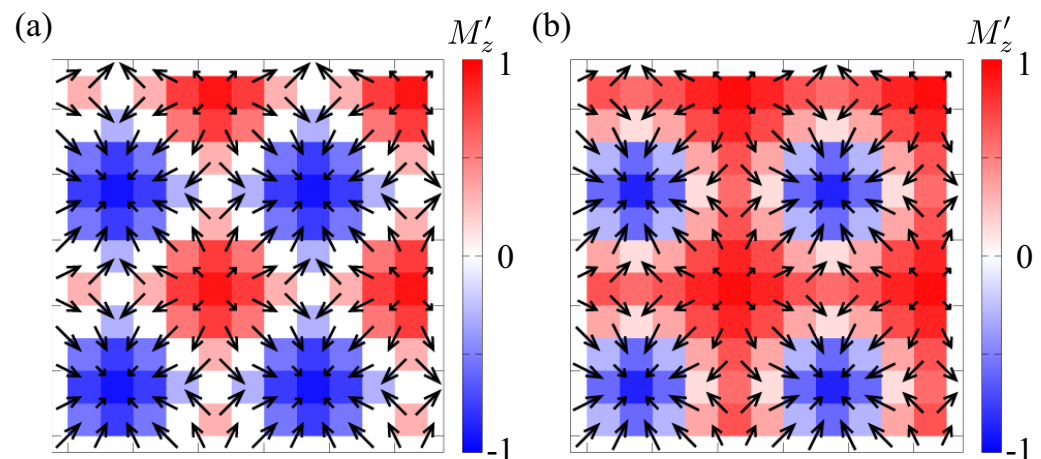
Figure 1. The real-space spin configurations in (**a**) the Néel-type vortex crystal and (**b**) the Néel-type skyrmion crystal. The arrows represent the direction of the spin moments while the contour shows the z-spin component M_z'.

The different types of vortex and skyrmion crystals are obtained by changing the in-plane spin components in Equation (3). The Bloch-type vortex and skyrmion spin textures with different helicities from the Néel-type ones are provided by

$$\boldsymbol{M}_i' = \mathcal{N}_i \begin{pmatrix} \cos \boldsymbol{Q}_2 \cdot \boldsymbol{r}_i \\ -\cos \boldsymbol{Q}_1 \cdot \boldsymbol{r}_i \\ \tilde{M}_z - \sin \boldsymbol{Q}_1 \cdot \boldsymbol{r}_i - \sin \boldsymbol{Q}_2 \cdot \boldsymbol{r}_i \end{pmatrix}^{\mathrm{T}}, \tag{4}$$

where the skyrmion number is also characterized by -1 owing to the same vorticity. The spin configurations of the Bloch-type vortex and skyrmion crystals are shown in Figure 2a and Figure 2b, respectively. Similarly, we can define the spin textures for two types of anti-type vortex and skyrmion spin textures with skyrmion number $+1$, i.e., with different vorticities from the Néel-type and Bloch-type ones. The spin ansatz of type-I anti-vortex and anti-skyrmion crystals is provided by

$$\boldsymbol{M}_i' = \mathcal{N}_i \begin{pmatrix} \cos \boldsymbol{Q}_2 \cdot \boldsymbol{r}_i \\ \cos \boldsymbol{Q}_1 \cdot \boldsymbol{r}_i \\ \tilde{M}_z - \sin \boldsymbol{Q}_1 \cdot \boldsymbol{r}_i - \sin \boldsymbol{Q}_2 \cdot \boldsymbol{r}_i \end{pmatrix}^{\mathrm{T}}, \tag{5}$$

while that of type-II anti-vortex and anti-skyrmion crystals is provided by

$$\boldsymbol{M}_i' = \mathcal{N}_i \begin{pmatrix} -\cos \boldsymbol{Q}_1 \cdot \boldsymbol{r}_i \\ \cos \boldsymbol{Q}_2 \cdot \boldsymbol{r}_i \\ \tilde{M}_z - \sin \boldsymbol{Q}_1 \cdot \boldsymbol{r}_i - \sin \boldsymbol{Q}_2 \cdot \boldsymbol{r}_i \end{pmatrix}^{\mathrm{T}}. \tag{6}$$

The spin configurations corresponding to these anti-type vortex and skyrmion crystals are presented in Figure 2c–f. Furthermore, we can define hybrid vortex and skyrmion crystals which consist of a linear combination of the Néel-type and Bloch-type spin textures. The spin configurations of such hybrid vortex and skyrmion crystals are shown in Figure 2g and Figure 2h, respectively.
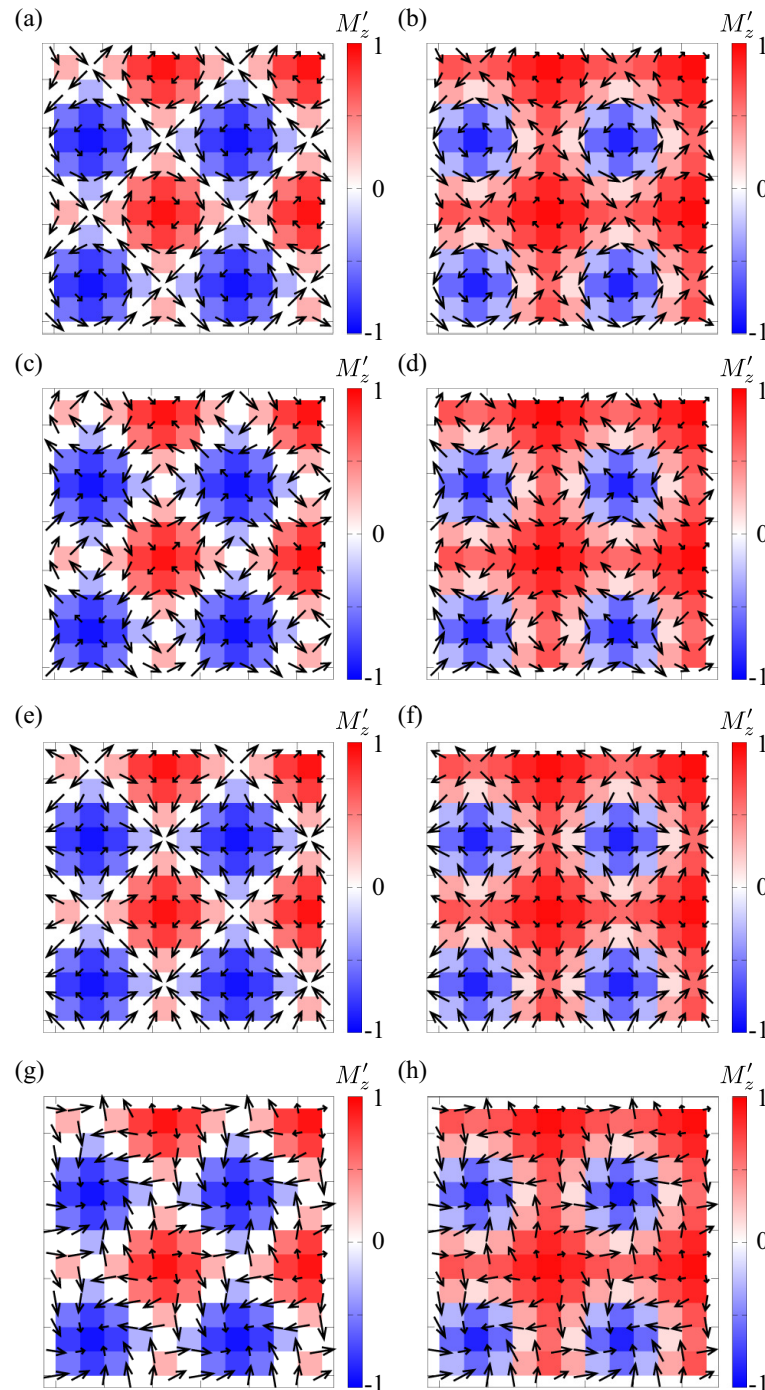
Figure 2. The real-space spin configurations in (**a**) the Bloch-type vortex crystal, (**b**) Bloch-type skyrmion crystal, (**c**) type-I anti-vortex crystal, (**d**) type-I anti-skyrmion crystal, (**e**) type-II anti-vortex crystal, (**f**) type-II anti-skyrmion crystal, (**g**) hybrid vortex crystal, and (**h**) hybrid skyrmion crystal. The arrows represent the direction of the spin moments, while the contour shows the z-spin component M'_z.

From the viewpoint of stability, the double-Q vortex and skyrmion crystals are stabilized when taking into account the effect of the Dzyaloshinskii–Moriya interaction in non-centrosymmetric lattice structures [88,89] or frustrated and multiple-spin interactions in centrosymmetric lattice structures [81,90–92]. Especially in the latter mechanism, the Néel-type, Bloch-type, and anti-type vortex and skyrmion crystals are energetically degenerated when the effect of the spin–orbit coupling is ignored [93]. This degeneracy is lifted by the magnetic anisotropy arising from the interplay between the spin–orbit coupling and the crystalline electric field [94]. For example, the magnetic anisotropy under C_{4h} symmetry favors hybrid vortex and skyrmion crystals [95]. Double-Q skyrmion crystals have been found in both non-centrosymmetric materials such as $Co_{10-x/2}Zn_{10-x/2}Mn_x$ [96–100] and Cu_2OSeO_3 [101,102] and in centrosymmetric materials such as $GdRu_2Si_2$ [103–107].

3. Results

3.1. Néel-Type Vortex Crystal

First, we discuss the result in the case of the Néel-type vortex crystal by setting $\tilde{M}_z = 0$ in Equation (3). We diagonalize the Hamiltonian in Equation (1) for the $N = 6 \times 6$ spins under the periodic boundary conditions; we also consider the 200×200 supercells in order to reduce the finite-size effect. Figures 3 and 4 show the electric-type and magnetic-type multipole structure factors at $\mu = 0$ (μ represents the chemical potential), respectively. The multipole structure factor is defined as

$$\tilde{X}(\boldsymbol{q}) = \frac{1}{N} \sum_{ij} \langle X \rangle_i \langle X \rangle_j e^{i\boldsymbol{q}\cdot(\boldsymbol{r}_i - \boldsymbol{r}_j)}, \tag{7}$$

where X represents all the multipoles activated in the s–p hybridized system. Because the multipoles belonging to the same irreducible representation under the D_{4h} point group show qualitatively similar profiles in the multipole structure factor, we plot one of the multipole structure factors in each irreducible representation in Figures 3 and 4: the data in Figure 3a–l correspond to those in the A_{1g}^+, A_{2g}^+, B_{1g}^+, B_{2g}^+, two E_g^+, A_{1u}^+, A_{2u}^+, B_{1u}^+, B_{2u}^+, and two E_u^+ irreducible representations, respectively, the data in Figure 4a–l correspond to those in the A_{1g}^-, A_{2g}^-, B_{1g}^-, B_{2g}^-, two E_g^-, A_{1u}^-, A_{2u}^-, B_{1u}^-, B_{2u}^-, and two E_u^- irreducible representations, respectively, and the superscript of the irreducible representation stands for the parity in terms of the time-reversal operations. The correspondence between the irreducible representations and multipoles is summarized in Table 2. In addition, we show the real-space electric-type and magnetic-type multipole configurations in Figures A1 and A2, respectively, in Appendix B for reference.

Under the Néel-type vortex crystal, the magnetic point group reduces from $4/mmm1'$ to $4mm1'$. It is notable that the time-reversal symmetry is not broken under the Néel-type vortex crystal, as the magnetic texture is invariant for the product of the time-reversal and translational operations. Thus, the uniform component of the magnetic-type multipoles is not induced in the Néel-type vortex crystal. Meanwhile, the symmetries with respect to the spatial inversion, the mirror in the horizontal plane, and the C_2 rotation around the x axis are broken, which indicates that the A_{2u}^+ irreducible representation corresponds to the order parameter. Because the electric dipoles Q_z and $Q_z^{(s)}$ belong to the A_{2u}^+ irreducible representation, they are regarded as the multipole order parameter of the Néel-type vortex crystal. According to symmetry reduction, electric dipole-related physical phenomena such as Rashba-type antisymmetric spin splitting in the band structure [108–111] and the transverse Edelstein effect [41] are expected.

Table 2. Symmetry reduction from the magnetic point group $4/mmm1'$ to $4mm1'$ when the double-Q Néel-type vortex crystal occurs in Equation (3). The correspondence among the irreducible representation (Irrep.), multipole (MP), and main peak positions in the multipole structure factor is presented. The upper (lower) panel represents the electric-type (magnetic-type) multipoles. In the spinful basis, the irreducible representations $(A_{1g}, A_{2g}, B_{1g}, B_{2g}, E_g, A_{1u}, A_{2u}, B_{1u}, B_{2u}, E_u)$ are replaced by $(E_{1/2g}, E_{1/2g}, E_{3/2g}, E_{3/2g}, E_{1/2g} \oplus E_{3/2g}, E_{1/2u}, E_{1/2u}, E_{3/2u}, E_{3/2u}, E_{1/2u} \oplus E_{3/2u})$.
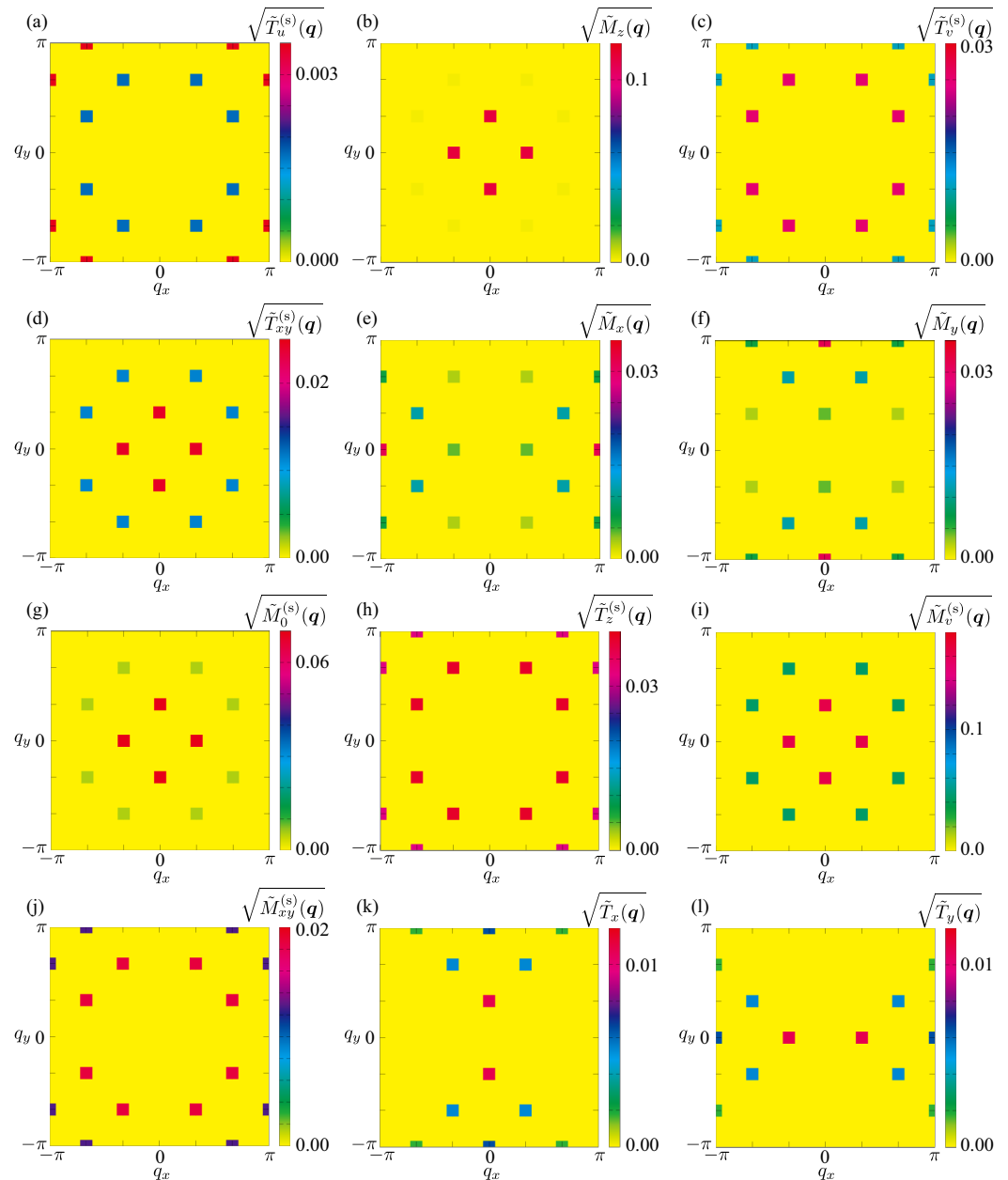
Irrep.	MP	Peak Positions
$A_{1g}^+ \to A_1^+$	$Q_{s,0}, Q_{p,0}, Q_0^{(s)}, Q_u, Q_u^{(s)}$	$\mathbf{0}, \mathbf{Q}_1 \pm \mathbf{Q}_2, 2\mathbf{Q}_{1,2}$
$A_{2g}^+ \to A_2^+$	$G_z^{(s)}$	$3\mathbf{Q}_1 \pm \mathbf{Q}_2, 3\mathbf{Q}_2 \pm \mathbf{Q}_1$
$B_{1g}^+ \to B_1^+$	$Q_v, Q_v^{(s)}$	$2\mathbf{Q}_{1,2}$
$B_{2g}^+ \to B_2^+$	$Q_{xy}, Q_{xy}^{(s)}$	$\mathbf{Q}_1 \pm \mathbf{Q}_2, 2\mathbf{Q}_1 \pm 2\mathbf{Q}_2$
$E_g^+ \to E^+$	$(Q_{yz}, Q_{zx}), (Q_{yz}^{(s)}, Q_{zx}^{(s)}), (G_x^{(s)}, G_y^{(s)})$	$\mathbf{Q}_1 \pm \mathbf{Q}_2, 2\mathbf{Q}_{1,2}$
$A_{1u}^+ \to A_2^+$	$G_0^{(s)}, G_u^{(s)}$	$3\mathbf{Q}_1 \pm \mathbf{Q}_2, 3\mathbf{Q}_2 \pm \mathbf{Q}_1$
$A_{2u}^+ \to A_1^+$	$Q_z, Q_z^{(s)}$	$\mathbf{0}, \mathbf{Q}_1 \pm \mathbf{Q}_2, 2\mathbf{Q}_{1,2}$
$B_{1u}^+ \to B_2^+$	$G_v^{(s)}$	$\mathbf{Q}_1 \pm \mathbf{Q}_2, 2\mathbf{Q}_1 \pm 2\mathbf{Q}_2$
$B_{2u}^+ \to B_1^+$	$G_{xy}^{(s)}$	$2\mathbf{Q}_{1,2}$
$E_u^+ \to E^+$	$(Q_x, Q_y), (Q_x^{(s)}, Q_y^{(s)}), (G_{yz}^{(s)}, G_{zx}^{(s)})$	$\mathbf{Q}_1 \pm \mathbf{Q}_2, 2\mathbf{Q}_{1,2}$
$A_{1g}^- \to A_1^-$	$T_u^{(s)}$	$2\mathbf{Q}_1 \pm \mathbf{Q}_2, 2\mathbf{Q}_2 \pm \mathbf{Q}_1$
$A_{2g}^- \to A_2^-$	$M_z, M_{s,z}^{(s)}, M_{p,z}^{(s)}, M_{a,z}^{(s)}, M_z^{\alpha(s)}$	$\mathbf{Q}_{1,2}, 2\mathbf{Q}_1 \pm \mathbf{Q}_2, 2\mathbf{Q}_2 \pm \mathbf{Q}_1$
$B_{1g}^- \to B_1^-$	$T_v^{(s)}, M_{xyz}^{(s)}$	$2\mathbf{Q}_1 \pm \mathbf{Q}_2, 2\mathbf{Q}_2 \pm \mathbf{Q}_1$
$B_{2g}^- \to B_2^-$	$T_{xy}^{(s)}, M_z^{\beta(s)}$	$\mathbf{Q}_{1,2}, 2\mathbf{Q}_1 \pm \mathbf{Q}_2, 2\mathbf{Q}_2 \pm \mathbf{Q}_1$
$E_g^- \to E^-$	$(M_x, M_y), (M_{s,x}^{(s)}, M_{s,y}^{(s)}), (M_{p,x}^{(s)}, M_{p,y}^{(s)}), (M_{a,x}^{(s)}, M_{a,y}^{(s)}),$ $(T_{yz}^{(s)}, T_{zx}^{(s)}), (M_x^{\alpha(s)}, M_y^{\alpha(s)}), (M_x^{\beta(s)}, M_y^{\beta(s)})$	$\mathbf{Q}_{1,2}, 2\mathbf{Q}_1 \pm \mathbf{Q}_2, 2\mathbf{Q}_2 \pm \mathbf{Q}_1$
$A_{1u}^- \to A_2^-$	$M_0^{(s)}, M_u^{(s)}$	$\mathbf{Q}_{1,2}, 2\mathbf{Q}_1 \pm \mathbf{Q}_2, 2\mathbf{Q}_2 \pm \mathbf{Q}_1$
$A_{2u}^- \to A_1^-$	$T_z, T_z^{(s)}$	$2\mathbf{Q}_1 \pm \mathbf{Q}_2, 2\mathbf{Q}_2 \pm \mathbf{Q}_1$
$B_{1u}^- \to B_2^-$	$M_v^{(s)}$	$\mathbf{Q}_{1,2}, 2\mathbf{Q}_1 \pm \mathbf{Q}_2, 2\mathbf{Q}_2 \pm \mathbf{Q}_1$
$B_{2u}^- \to B_1^-$	$M_{xy}^{(s)}$	$2\mathbf{Q}_1 \pm \mathbf{Q}_2, 2\mathbf{Q}_2 \pm \mathbf{Q}_1$
$E_u^- \to E^-$	$(T_x, T_y), (T_x^{(s)}, T_y^{(s)}), (M_{yz}^{(s)}, M_{zx}^{(s)})$	$\mathbf{Q}_{1,2}, 2\mathbf{Q}_1 \pm \mathbf{Q}_2, 2\mathbf{Q}_2 \pm \mathbf{Q}_1$

In addition, we find that finite-q modulations, i.e., density waves, are induced in each multipole channel, as shown in Figures 3 and 4. The nonzero modulations for the wave vector $\mathbf{q}$ are understood from the effective coupling between multipoles and spin configurations [112]. For example, the $\mathbf{q}$ component of the electric quadrupole $Q_v \propto x^2 - y^2$ is coupled to the spins as $(S_{q_1}^x S_{q_2}^x - S_{q_1}^y S_{q_2}^y)\delta_{q_1+q_2+q,0}$ in the lowest-order approximation, where δ is the Kronecker delta. From Equation (3), the above quantity becomes nonzero for $\mathbf{q}_1 = \mathbf{Q}_1$, $\mathbf{q}_2 = \mathbf{Q}_1$, and $\mathbf{q} = -2\mathbf{Q}_1$ (or $\mathbf{q}_1 = \mathbf{Q}_2$, $\mathbf{q}_2 = \mathbf{Q}_2$, and $\mathbf{q} = -2\mathbf{Q}_2$). This is why the intensities at $2\mathbf{Q}_1$ and $2\mathbf{Q}_2$ appear in $\tilde{Q}_v(\mathbf{q})$. Similarly, the $\mathbf{q}$ component of the electric quadrupole $Q_{xy} \propto xy$ is coupled to $S_{q_1}^x S_{q_2}^y \delta_{q_1+q_2+q,0}$, which leads to the intensities at $\mathbf{Q}_1 \pm \mathbf{Q}_2$ in $\tilde{Q}_{xy}(\mathbf{q})$. In this way, the finite-q peak positions in the multipole structure factor are accounted for by the two or higher-order spin-scattering processes.
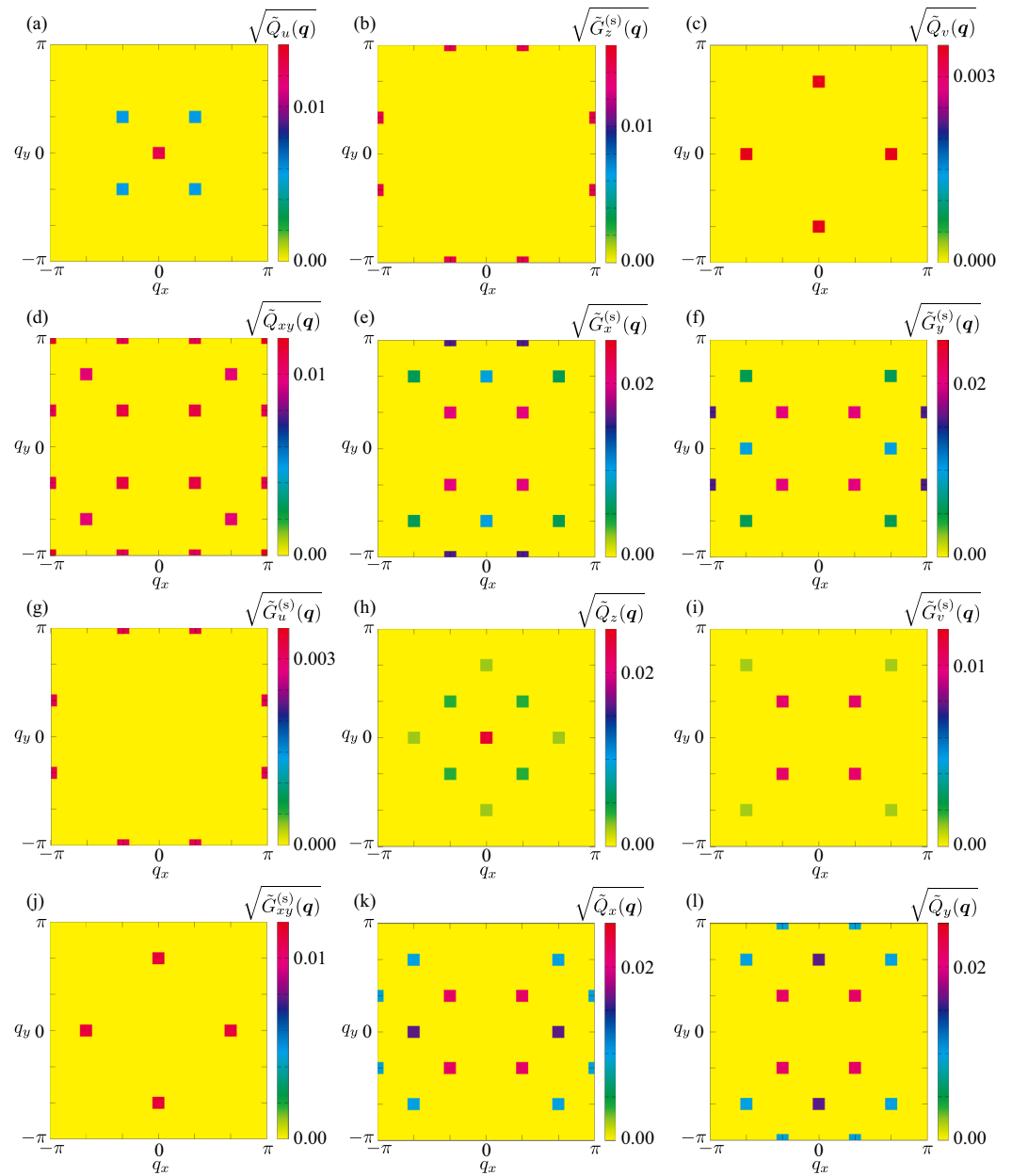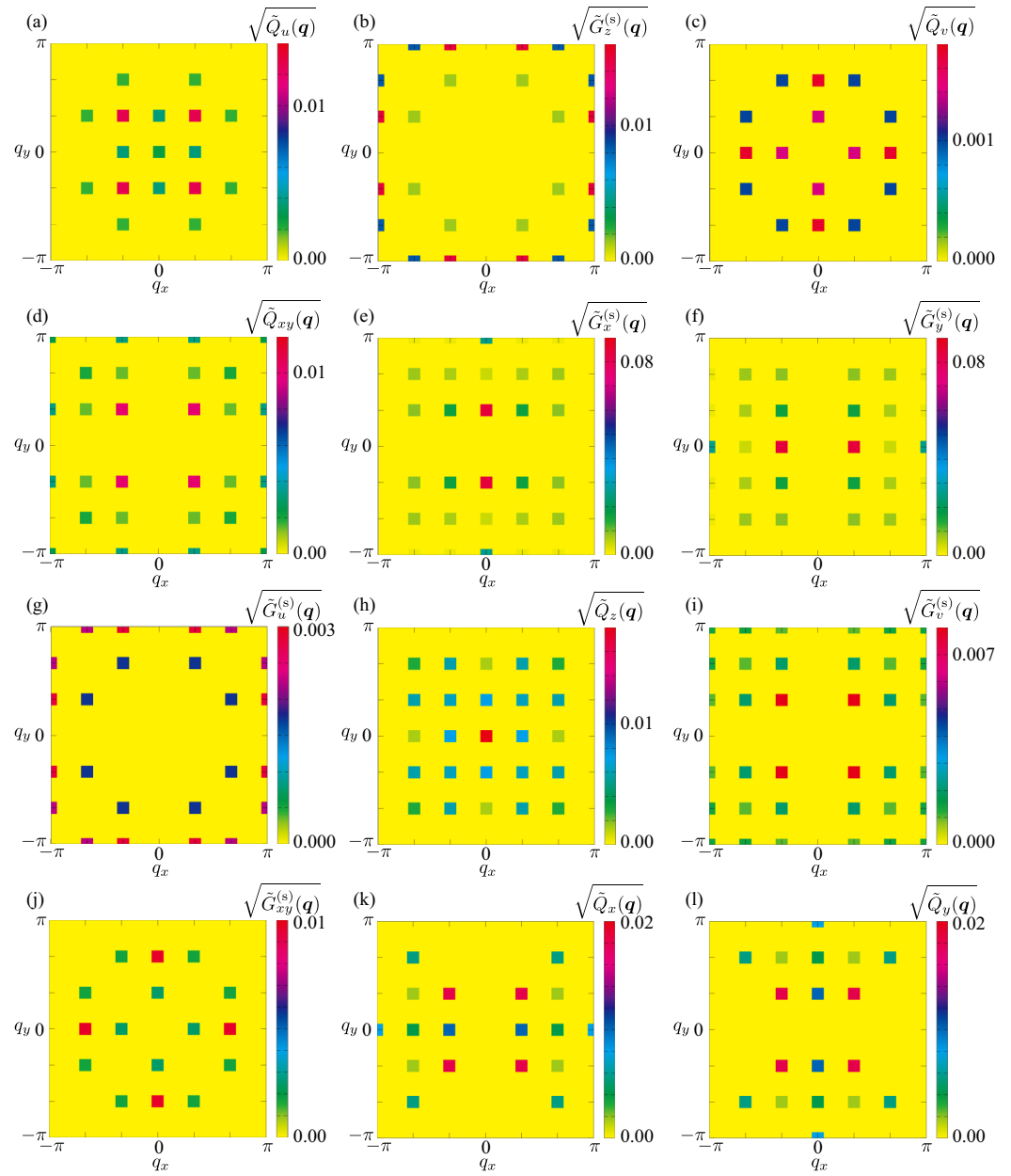
Figure 3. The square root of the electric-type multipole structure factor in the Néel-type vortex crystal for (**a**) $\tilde{Q}_u(\boldsymbol{q})$, (**b**) $\tilde{G}_z^{(\mathrm{s})}(\boldsymbol{q})$, (**c**) $\tilde{Q}_v(\boldsymbol{q})$, (**d**) $\tilde{Q}_{xy}(\boldsymbol{q})$, (**e**) $\tilde{G}_x^{(\mathrm{s})}(\boldsymbol{q})$, (**f**) $\tilde{G}_y^{(\mathrm{s})}(\boldsymbol{q})$, (**g**) $\tilde{G}_u^{(\mathrm{s})}(\boldsymbol{q})$, (**h**) $\tilde{Q}_z(\boldsymbol{q})$, (**i**) $\tilde{G}_v^{(\mathrm{s})}(\boldsymbol{q})$, (**j**) $\tilde{G}_{xy}^{(\mathrm{s})}(\boldsymbol{q})$, (**k**) $\tilde{Q}_x(\boldsymbol{q})$, and (**l**) $\tilde{Q}_y(\boldsymbol{q})$.

Figure 4. The square root of the magnetic-type multipole structure factor in the Néel-type vortex crystal for (**a**) $\tilde{T}_u^{(s)}(\boldsymbol{q})$, (**b**) $\tilde{M}_z(\boldsymbol{q})$, (**c**) $\tilde{T}_v^{(s)}(\boldsymbol{q})$, (**d**) $\tilde{T}_{xy}^{(s)}(\boldsymbol{q})$, (**e**) $\tilde{M}_x(\boldsymbol{q})$, (**f**) $\tilde{M}_y(\boldsymbol{q})$, (**g**) $\tilde{M}_0^{(s)}(\boldsymbol{q})$, (**h**) $\tilde{T}_z^{(s)}(\boldsymbol{q})$, (**i**) $\tilde{M}_v^{(s)}(\boldsymbol{q})$, (**j**) $\tilde{M}_{xy}^{(s)}(\boldsymbol{q})$, (**k**) $\tilde{T}_x(\boldsymbol{q})$, and (**l**) $\tilde{T}_y(\boldsymbol{q})$.

3.2. Néel-Type Skyrmion Crystal

Next, we consider the Néel-type skyrmion crystal by setting $\tilde{M}_z = 0.5$ in Equation (3). Figures 5 and 6 represent the electric-type and magnetic-type multipole structure factors, respectively. Owing to the presence of uniform magnetization, the symmetry in the Néel-type skyrmion crystal is further reduced from $4mm1'$ in the Néel-type vortex crystal to $4m'm'$. In addition to A_{2u}^+, the A_{2g}^- and A_{1u}^- irreducible representations belong to the identity irreducible representation, as shown in Table 3. In other words, the uniform component of the magnetic monopole M_0 is induced, as shown in Figure 6g. Thus, the longitudinal magnetoelectric effect, which is caused by M_0, is expected in the Néel-type skyrmion crystal. Compared to the result in the Néel-type vortex crystal, the number of peak positions in the multipole structure factor increases in the Néel-type skyrmion crystal. This is because of the additional coupling between the multipoles and spin textures owing to the $\boldsymbol{q} = \boldsymbol{0}$ component. For example, in the case of $\tilde{Q}_v(\boldsymbol{q})$, the $\boldsymbol{Q}_1$ and $\boldsymbol{Q}_2$ components are additionally

induced, as $(S^x_{q_1} S^x_{q_2} - S^y_{q_1} S^y_{q_2})\delta_{q_1+q_2+q,0}$ becomes nonzero for $q_1 = Q_1 + Q_2$, $q_2 = -Q_2$, and $q = -Q_1$ (or $q_1 = Q_1 + Q_2$, $q_2 = -Q_1$, and $q = -Q_2$). It is notable that $S^x_{Q_1+Q_2}$ and $S^y_{Q_1+Q_2}$ become nonzero only for $\tilde{M}_z \neq 0$, as shown in Figures 4e,f and 6e,f. The emergent multipole moments in the vortex and skyrmion crystal are consistent with the symmetry argument under magnetic point groups [71].

Figure 5. The square root of the electric-type multipole structure factor in the Néel-type skyrmion crystal for (**a**) $\tilde{Q}_u(q)$, (**b**) $\tilde{G}^{(s)}_z(q)$, (**c**) $\tilde{Q}_v(q)$, (**d**) $\tilde{Q}_{xy}(q)$, (**e**) $\tilde{G}^{(s)}_x(q)$, (**f**) $\tilde{G}^{(s)}_y(q)$, (**g**) $\tilde{G}^{(s)}_u(q)$, (**h**) $\tilde{Q}_z(q)$, (**i**) $\tilde{G}^{(s)}_v(q)$, (**j**) $\tilde{G}^{(s)}_{xy}(q)$, (**k**) $\tilde{Q}_x(q)$, and (**l**) $\tilde{Q}_y(q)$.
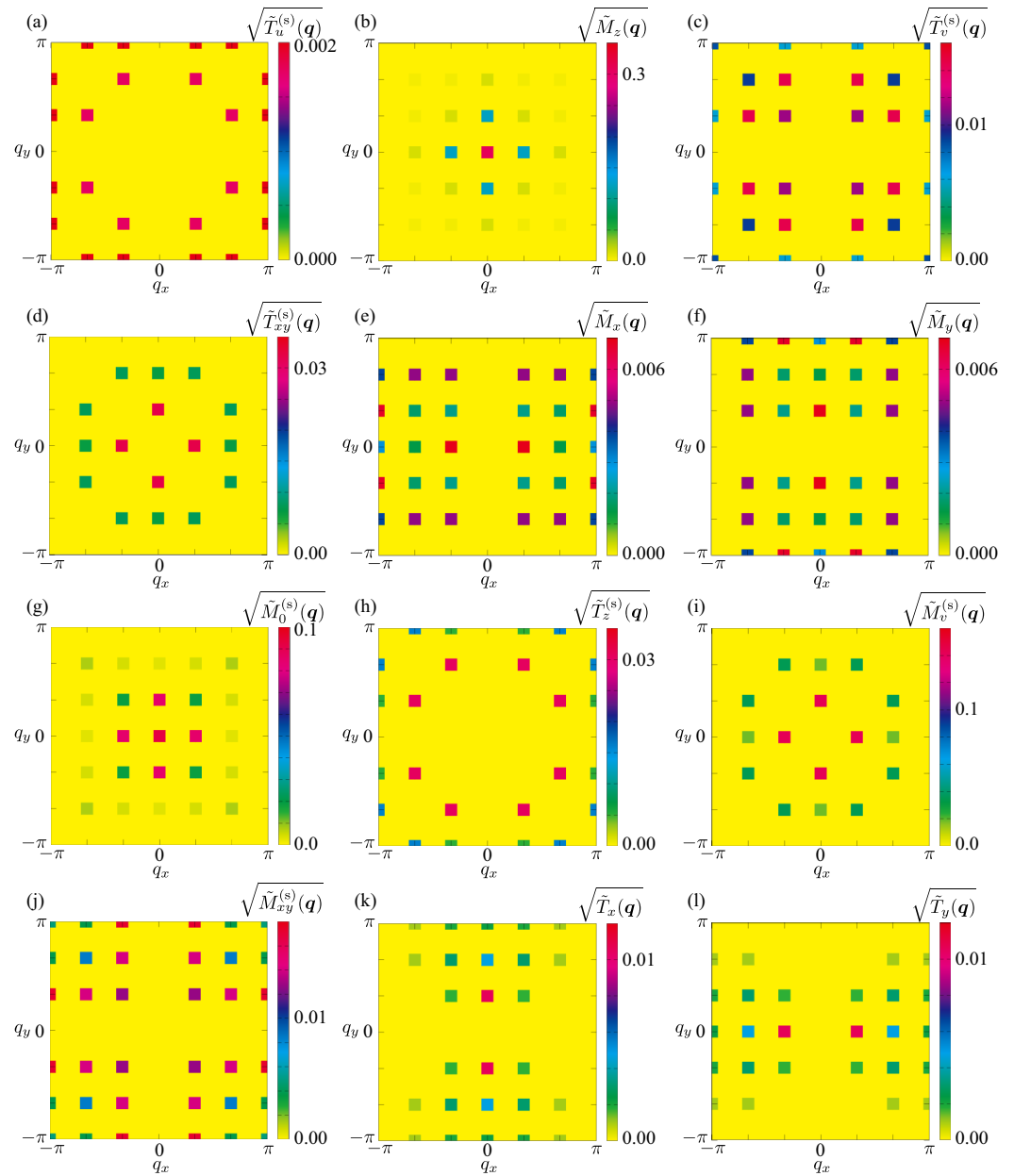
Figure 6. The square root of the magnetic-type multipole structure factor in the Néel-type skyrmion crystal for (**a**) $\tilde{T}_u^{(s)}(\boldsymbol{q})$, (**b**) $\tilde{M}_z(\boldsymbol{q})$, (**c**) $\tilde{T}_v^{(s)}(\boldsymbol{q})$, (**d**) $\tilde{T}_{xy}^{(s)}(\boldsymbol{q})$, (**e**) $\tilde{M}_x(\boldsymbol{q})$, (**f**) $\tilde{M}_y(\boldsymbol{q})$, (**g**) $\tilde{M}_0^{(s)}(\boldsymbol{q})$, (**h**) $\tilde{T}_z^{(s)}(\boldsymbol{q})$, (**i**) $\tilde{M}_v^{(s)}(\boldsymbol{q})$, (**j**) $\tilde{M}_{xy}^{(s)}(\boldsymbol{q})$, (**k**) $\tilde{T}_x(\boldsymbol{q})$, and (**l**) $\tilde{T}_y(\boldsymbol{q})$.

Table 3. Symmetry reduction from the magnetic point group $4/mmm1'$ to $4m'm'$ when the double-Q Néel-type skyrmion crystal occurs in Equation (3). The correspondence among the irreducible representation (Irrep.), multipole (MP), and main peak positions in the multipole structure factor is presented. The upper (lower) panel represents the electric-type (magnetic-type) multipoles.

Irrep.	MP	Peak Positions
$A_{1g}^+ \to A^+$	$Q_{s,0}, Q_{p,0}, Q_0^{(s)}, Q_u, Q_u^{(s)}$	$\mathbf{0}, Q_{1,2}, Q_1 \pm Q_2$
$A_{2g}^+ \to A^-$	$G_z^{(s)}$	$2Q_1 \pm Q_2, 2Q_2 \pm Q_1$
$B_{1g}^+ \to B^+$	$Q_v, Q_v^{(s)}$	$Q_{1,2}, 2Q_{1,2}$
$B_{2g}^+ \to B^-$	$Q_{xy}, Q_{xy}^{(s)}$	$Q_1 \pm Q_2, 2Q_1 \pm 2Q_2$
$E_g^+ \to E^{(1,2)+}$	$(Q_{yz}, Q_{zx}), (Q_{yz}^{(s)}, Q_{zx}^{(s)}), (G_x^{(s)}, G_y^{(s)})$	$Q_{1,2}, Q_1 \pm Q_2$
$A_{1u}^+ \to A^-$	$G_0^{(s)}, G_u^{(s)}$	$2Q_1 \pm Q_2, 2Q_2 \pm Q_1$
$A_{2u}^+ \to A^+$	$Q_z, Q_z^{(s)}$	$\mathbf{0}, Q_{1,2}, Q_1 \pm Q_2$
$B_{1u}^+ \to B^-$	$G_v^{(s)}$	$Q_1 \pm Q_2, 2Q_1 \pm 2Q_2$
$B_{2u}^+ \to B^+$	$G_{xy}^{(s)}$	$Q_{1,2}, 2Q_{1,2}$
$E_u^+ \to E^{(1,2)-}$	$(Q_x, Q_y), (Q_x^{(s)}, Q_y^{(s)}), (G_{yz}^{(s)}, G_{zx}^{(s)})$	$Q_{1,2}, Q_1 \pm Q_2$
$A_{1g}^- \to A^-$	$T_u^{(s)}$	$2Q_1 \pm Q_2, 2Q_1 \pm Q_2$
$A_{2g}^- \to A^+$	$M_z, M_{s,z}^{(s)}, M_{p,z}^{(s)}, M_{a,z}^{(s)}, M_z^{\alpha(s)}$	$\mathbf{0}, Q_{1,2}, Q_1 \pm Q_2$
$B_{1g}^- \to B^-$	$T_v^{(s)}, M_{xyz}^{(s)}$	$Q_1 \pm Q_2, 2Q_2 \pm 2Q_1$
$B_{2g}^- \to B^+$	$T_{xy}^{(s)}, M_z^{\beta(s)}$	$Q_{1,2}, 2Q_{1,2}$
$E_g^- \to E^{(1,2)-}$	$(M_x, M_y), (M_{s,x}^{(s)}, M_{s,y}^{(s)}), (M_{p,x}^{(s)}, M_{p,y}^{(s)}), (M_{a,x}^{(s)}, M_{a,y}^{(s)}),$ $(T_{yz}^{(s)}, T_{zx}^{(s)}), (M_x^{\alpha(s)}, M_y^{\alpha(s)}), (M_x^{\beta(s)}, M_y^{\beta(s)})$	$Q_{1,2}, Q_1 \pm Q_2$
$A_{1u}^- \to A^+$	$M_0^{(s)}, M_u^{(s)}$	$\mathbf{0}, Q_{1,2}, Q_1 \pm Q_2$
$A_{2u}^- \to A^-$	$T_z, T_z^{(s)}$	$2Q_1 \pm Q_2, 2Q_2 \pm Q_1$
$B_{1u}^- \to B^+$	$M_v^{(s)}$	$Q_{1,2}, 2Q_{1,2}$
$B_{2u}^- \to B^-$	$M_{xy}^{(s)}$	$Q_1 \pm Q_2, 2Q_1 \pm 2Q_2$
$E_u^- \to E^{(1,2)+}$	$(T_x, T_y), (T_x^{(s)}, T_y^{(s)}), (M_{yz}^{(s)}, M_{zx}^{(s)})$	$Q_{1,2}, Q_1 \pm Q_2$

3.3. Other Vortex and Skyrmion Types

In this subsection, we discuss the multipole moments induced by other types of vortex and skyrmion crystals. For the Bloch-type vortex crystal in Figure 2a, the electric toroidal monopole G_0 and electric toroidal quadrupole G_u are induced instead of Q_z in the Néel-type vortex crystal. Because these multipoles are related to chirality, the Bloch-type vortex crystal exhibits the chirality-related physical phenomena, such as antisymmetric spin splitting in the form of $c_1(k_x\sigma_x + k_y\sigma_y) + c_2 k_z\sigma_z$ (c_1 and c_2 are numerical coefficients) and the longitudinal Edelstein effect. When the effect of the magnetic field is taken into account, the Bloch-type vortex crystal turns into the Bloch-type skyrmion crystal in Figure 2b, where the magnetic toroidal dipole T_z is additionally induced. Thus, the nonreciprocal transport along the z direction and the linear transverse magnetoelectric effect are expected to occur.

In the cases of the type-I and type-II anti-vortex crystals in Figure 2c,e, the rank-2 electric toroidal quadrupoles G_v and G_{xy} [113] are induced, which exhibit antisymmetric spin splittings in the functional forms of $k_x\sigma_x - k_y\sigma_y$ and $k_x\sigma_y + k_y\sigma_x$, respectively. When the type-I and type-II anti-skyrmion crystals in Figure 2d,f are realized under the external magnetic field, the magnetic quadrupoles M_{xy} and M_v are induced, both of which become the origin of the linear magnetoelectric effect, although the tensor components are different from those under M_0 and T_z.

Finally, further multipole moments can be induced when the hybrid vortex and skyrmion crystals in Figure 2g,h are considered. In this case, the electric toroidal dipole G_z is additionally induced owing to the simultaneous appearance of M_0 and T_z, which becomes the origin of the rotational responses between conjugate fields and physical

quantities with the same symmetry, such as the spin current generation [68]. A similar situation happens for anti-hybrid vortex (skyrmion) crystals consisting of a superposition of type-I and type-II anti-vortex (anti-skyrmion) crystals. We summarize the induced multipole moments under different types of vortex and skyrmion crystals in Table 4.

Table 4. Uniform component of multipole moments induced by vortex and skyrmion crystals with different vorticities and helicities; H represents the magnetic field and MPG stands for the magnetic point group. The multipoles are classified according to their spatial inversion ($\mathcal{P}$) and time-reversal ($\mathcal{T}$) parities.

Type	H	MPG	$(\mathcal{P}, \mathcal{T})$			
			$(+1, +1)$	$(-1, +1)$	$(+1, -1)$	$(-1, -1)$
para	$= 0$	$4/mmm1'$	Q_0, Q_u			
Bloch	$= 0$	$4221'$		G_0, G_u		
	$\neq 0$	$42'2'$		G_0, G_u	M_z, M_z^α	T_z
Néel	$= 0$	$4mm1'$		Q_z		
	$\neq 0$	$4m'm'$		Q_z	M_z, M_z^α	M_0, M_u
anti-I	$= 0$	$\bar{4}2m1'$		G_v		
	$\neq 0$	$\bar{4}2'm'$		G_v	M_z, M_z^α	M_{xy}
anti-II	$= 0$	$\bar{4}m21'$		G_{xy}		
	$\neq 0$	$\bar{4}m'2'$		G_{xy}	M_z, M_z^α	M_v
hybrid	$= 0$	$41'$	G_z	G_0, Q_z, G_u		
	$\neq 0$	4	G_z	G_0, Q_z, G_u	M_z, T_u, M_z^α	M_0, T_z, M_u
anti-hybrid	$= 0$	$\bar{4}1'$	G_z	G_v, G_{xy}		
	$\neq 0$	$\bar{4}$	G_z	G_v, G_{xy}	M_z, T_u, M_z^α	M_v, T_{xy}

4. Conclusions

In this paper, we have investigated the relationship between multipole moments and topologically nontrivial spin textures. By introducing four types of multipoles (electric, magnetic, magnetic toroidal, and electric toroidal), we have shown that different types of multipoles are induced by various types of vortex and skyrmion crystals with different vorticities and helicities under tetragonal symmetry. In addition, we have classified the induced multipole moments in terms of the uniform and finite-q components. Because different multipoles give rise to different physical properties, rich physics can be expected in non-coplanar multiple-q states with various multipole moments, which can stimulate the future exploration of functional magnetic materials.

Data Availability Statement: The data presented in this study are available on request from the corresponding author.

Conflicts of Interest: The author declares no conflicts of interest.

Appendix A. Matrix Elements of Multipoles

Below, we show the expressions of each multipole operator activated in the *s*–*p* hybridized system in matrix form [86]. By considering the atomic wave function for the *s* orbital as

$$\phi_0 = \frac{1}{\sqrt{4\pi}} \tag{A1}$$

and those for the three *p* orbitals as

$$\phi_{p_x} = \sqrt{\frac{3}{4\pi}}\frac{x}{r}, \quad \phi_{p_y} = \sqrt{\frac{3}{4\pi}}\frac{y}{r}, \quad \phi_{p_z} = \sqrt{\frac{3}{4\pi}}\frac{z}{r}, \tag{A2}$$

we can evaluate the multipole moments one by one.

In the spinless space, the matrix for the 16 multipoles, for which the basis is set for $(\phi_0, \phi_x, \phi_y, \phi_z)$, is provided by

$$
Q_{s,0} = \begin{pmatrix} 1 & 0 & 0 & 0 \\ \hline 0 & 0 & 0 & 0 \\ 0 & 0 & 0 & 0 \\ 0 & 0 & 0 & 0 \end{pmatrix}, \quad
Q_{p,0} = \begin{pmatrix} 0 & 0 & 0 & 0 \\ \hline 0 & 1 & 0 & 0 \\ 0 & 0 & 1 & 0 \\ 0 & 0 & 0 & 1 \end{pmatrix},
$$

$$
Q_x = \frac{1}{\sqrt{3}} \begin{pmatrix} 0 & 1 & 0 & 0 \\ \hline 1 & 0 & 0 & 0 \\ 0 & 0 & 0 & 0 \\ 0 & 0 & 0 & 0 \end{pmatrix}, \quad
Q_y = \frac{1}{\sqrt{3}} \begin{pmatrix} 0 & 0 & 1 & 0 \\ \hline 0 & 0 & 0 & 0 \\ 1 & 0 & 0 & 0 \\ 0 & 0 & 0 & 0 \end{pmatrix},
$$

$$
Q_z = \frac{1}{\sqrt{3}} \begin{pmatrix} 0 & 0 & 0 & 1 \\ \hline 0 & 0 & 0 & 0 \\ 0 & 0 & 0 & 0 \\ 1 & 0 & 0 & 0 \end{pmatrix}, \quad
\boldsymbol{Q} = (Q_x, Q_y, Q_z),
$$

$$
M_x = \begin{pmatrix} 0 & 0 & 0 & 0 \\ \hline 0 & 0 & 0 & 0 \\ 0 & 0 & 0 & -i \\ 0 & 0 & i & 0 \end{pmatrix}, \quad
M_y = \begin{pmatrix} 0 & 0 & 0 & 0 \\ \hline 0 & 0 & 0 & i \\ 0 & 0 & 0 & 0 \\ 0 & -i & 0 & 0 \end{pmatrix},
$$

$$
M_z = \begin{pmatrix} 0 & 0 & 0 & 0 \\ \hline 0 & 0 & -i & 0 \\ 0 & i & 0 & 0 \\ 0 & 0 & 0 & 0 \end{pmatrix}, \quad
\boldsymbol{M} = (M_x, M_y, M_z),
$$

$$
T_x = \frac{1}{3\sqrt{3}} \begin{pmatrix} 0 & i & 0 & 0 \\ \hline -i & 0 & 0 & 0 \\ 0 & 0 & 0 & 0 \\ 0 & 0 & 0 & 0 \end{pmatrix}, \quad
T_y = \frac{1}{3\sqrt{3}} \begin{pmatrix} 0 & 0 & i & 0 \\ \hline 0 & 0 & 0 & 0 \\ -i & 0 & 0 & 0 \\ 0 & 0 & 0 & 0 \end{pmatrix},
$$

$$
T_z = \frac{1}{3\sqrt{3}} \begin{pmatrix} 0 & 0 & 0 & i \\ \hline 0 & 0 & 0 & 0 \\ 0 & 0 & 0 & 0 \\ -i & 0 & 0 & 0 \end{pmatrix}, \quad
\boldsymbol{T} = (T_x, T_y, T_z),
$$

$$
Q_u = \frac{1}{5} \begin{pmatrix} 0 & 0 & 0 & 0 \\ \hline 0 & -1 & 0 & 0 \\ 0 & 0 & -1 & 0 \\ 0 & 0 & 0 & 2 \end{pmatrix}, \quad
Q_v = \frac{\sqrt{3}}{5} \begin{pmatrix} 0 & 0 & 0 & 0 \\ \hline 0 & 1 & 0 & 0 \\ 0 & 0 & -1 & 0 \\ 0 & 0 & 0 & 0 \end{pmatrix},
$$

$$
Q_{yz} = \frac{\sqrt{3}}{5} \begin{pmatrix} 0 & 0 & 0 & 0 \\ \hline 0 & 0 & 0 & 0 \\ 0 & 0 & 0 & 1 \\ 0 & 0 & 1 & 0 \end{pmatrix}, \quad
Q_{zx} = \frac{\sqrt{3}}{5} \begin{pmatrix} 0 & 0 & 0 & 0 \\ \hline 0 & 0 & 0 & 1 \\ 0 & 0 & 0 & 0 \\ 0 & 1 & 0 & 0 \end{pmatrix},
$$

$$
Q_{xy} = \frac{\sqrt{3}}{5} \begin{pmatrix} 0 & 0 & 0 & 0 \\ \hline 0 & 0 & 1 & 0 \\ 0 & 1 & 0 & 0 \\ 0 & 0 & 0 & 0 \end{pmatrix}. \tag{A3}
$$

In the spinful space, the matrix for the other 48 multipoles is obtained by the addition rule between the above spinless multipoles and the Pauli matrix $\sigma = (\sigma_x, \sigma_y, \sigma_z)$, which is provided by

$$Q_0^{(s)} = \frac{1}{\sqrt{3}}(M_x\sigma_x + M_y\sigma_y + M_z\sigma_z), \tag{A4}$$

$$\boldsymbol{Q}^{(s)} = \frac{1}{\sqrt{2}}(\boldsymbol{\sigma} \times \boldsymbol{T}), \tag{A5}$$

$$Q_u^{(s)} = \frac{1}{\sqrt{6}}(-M_x\sigma_x - M_y\sigma_y + 2M_z\sigma_z), \tag{A6}$$

$$Q_v^{(s)} = \frac{1}{\sqrt{2}}(M_x\sigma_x - M_y\sigma_y), \tag{A7}$$

$$Q_{yz}^{(s)} = \frac{1}{\sqrt{2}}(M_z\sigma_y + M_y\sigma_z), \tag{A8}$$

$$Q_{zx}^{(s)} = \frac{1}{\sqrt{2}}(M_z\sigma_x + M_x\sigma_z), \tag{A9}$$

$$Q_{xy}^{(s)} = \frac{1}{\sqrt{2}}(M_y\sigma_x + M_x\sigma_y), \tag{A10}$$

$$M_0^{(s)} = \frac{1}{\sqrt{3}}(Q_x\sigma_x + Q_y\sigma_y + Q_z\sigma_z), \tag{A11}$$

$$\boldsymbol{M}_s^{(s)} = Q_{s,0}\boldsymbol{\sigma}, \tag{A12}$$

$$\boldsymbol{M}_p^{(s)} = Q_{p,0}\boldsymbol{\sigma}, \tag{A13}$$

$$M_{a,x}^{(s)} = \sqrt{\frac{3}{10}}\left(-\frac{1}{\sqrt{3}}Q_u^{(-)}\sigma_x + Q_{xy}\sigma_y + Q_{zx}\sigma_z\right), \tag{A14}$$

$$M_{a,y}^{(s)} = \sqrt{\frac{3}{10}}\left(Q_{xy}\sigma_x - \frac{1}{\sqrt{3}}Q_u^{(+)}\sigma_y + Q_{yz}\sigma_z\right), \tag{A15}$$

$$M_{a,z}^{(s)} = \sqrt{\frac{3}{10}}\left(Q_{zx}\sigma_x + Q_{yz}\sigma_y + \frac{2}{\sqrt{3}}Q_u\sigma_z\right), \tag{A16}$$

$$M_u^{(s)} = \frac{1}{\sqrt{6}}(-Q_x\sigma_x - Q_y\sigma_y + 2Q_z\sigma_z), \tag{A17}$$

$$M_v^{(s)} = \frac{1}{\sqrt{2}}(Q_x\sigma_x - Q_y\sigma_y), \tag{A18}$$

$$M_{yz}^{(s)} = \frac{1}{\sqrt{2}}(Q_z\sigma_y + Q_y\sigma_z), \tag{A19}$$

$$M_{zx}^{(s)} = \frac{1}{\sqrt{2}}(Q_z\sigma_x + Q_x\sigma_z), \tag{A20}$$

$$M_{xy}^{(s)} = \frac{1}{\sqrt{2}}(Q_y\sigma_x + Q_x\sigma_y), \tag{A21}$$

$$M_{xyz}^{(s)} = \frac{1}{\sqrt{3}}(Q_{yz}\sigma_x + Q_{zx}\sigma_y + Q_{xy}\sigma_z), \tag{A22}$$

$$M_x^{\alpha(s)} = -\frac{1}{\sqrt{5}}\left(\frac{\sqrt{3}}{2}Q_u^{(-)}\sigma_x + Q_{xy}\sigma_y + Q_{zx}\sigma_z\right), \tag{A23}$$

$$M_y^{\alpha(s)} = -\frac{1}{\sqrt{5}}\left(Q_{xy}\sigma_x + \frac{\sqrt{3}}{2}Q_u^{(+)}\sigma_y + Q_{yz}\sigma_z\right), \tag{A24}$$

$$M_z^{\alpha(s)} = -\frac{1}{\sqrt{5}}(Q_{zx}\sigma_x + Q_{yz}\sigma_y - \sqrt{3}Q_u\sigma_z), \tag{A25}$$

$$M_x^{\beta(s)} = \frac{1}{\sqrt{3}}\left(-\frac{1}{2}Q_v^{(+)}\sigma_x + Q_{xy}\sigma_y - Q_{zx}\sigma_z\right), \tag{A26}$$

$$M_y^{\beta(\mathrm{s})} = \frac{1}{\sqrt{3}}\left(-Q_{xy}\sigma_x - \frac{1}{2}Q_v^{(-)}\sigma_y + Q_{yz}\sigma_z\right), \tag{A27}$$

$$M_z^{\beta(\mathrm{s})} = \frac{1}{\sqrt{3}}(Q_{zx}\sigma_x - Q_{yz}\sigma_y + Q_v\sigma_z), \tag{A28}$$

$$\boldsymbol{T}^{(\mathrm{s})} = \frac{1}{\sqrt{2}}(\boldsymbol{\sigma}\times\boldsymbol{Q}), \tag{A29}$$

$$T_u^{(\mathrm{s})} = \frac{1}{\sqrt{2}}(Q_{yz}\sigma_x - Q_{zx}\sigma_y), \tag{A30}$$

$$T_v^{(\mathrm{s})} = \frac{1}{\sqrt{6}}(Q_{yz}\sigma_x + Q_{zx}\sigma_y - 2Q_{xy}\sigma_z), \tag{A31}$$

$$T_{yz}^{(\mathrm{s})} = \frac{1}{\sqrt{6}}(-Q_v^{(+)}\sigma_x - Q_{xy}\sigma_y + Q_{zx}\sigma_z), \tag{A32}$$

$$T_{zx}^{(\mathrm{s})} = \frac{1}{\sqrt{6}}(Q_{xy}\sigma_x - Q_v^{(-)}\sigma_y - Q_{yz}\sigma_z), \tag{A33}$$

$$T_{xy}^{(\mathrm{s})} = \frac{1}{\sqrt{6}}(-Q_{zx}\sigma_x + Q_{yz}\sigma_y + 2Q_v\sigma_z), \tag{A34}$$

$$G_0^{(\mathrm{s})} = \frac{1}{\sqrt{3}}(T_x\sigma_x + T_y\sigma_y + T_z\sigma_z), \tag{A35}$$

$$\boldsymbol{G}^{(\mathrm{s})} = \frac{1}{\sqrt{2}}(\boldsymbol{\sigma}\times\boldsymbol{M}), \tag{A36}$$

$$G_u^{(\mathrm{s})} = \frac{1}{\sqrt{6}}(-T_x\sigma_x - T_y\sigma_y + 2T_z\sigma_z), \tag{A37}$$

$$G_v^{(\mathrm{s})} = \frac{1}{\sqrt{2}}(T_x\sigma_x - T_y\sigma_y), \tag{A38}$$

$$G_{yz}^{(\mathrm{s})} = \frac{1}{\sqrt{2}}(T_z\sigma_y + T_y\sigma_z), \tag{A39}$$

$$G_{zx}^{(\mathrm{s})} = \frac{1}{\sqrt{2}}(T_z\sigma_x + T_x\sigma_z), \tag{A40}$$

$$G_{xy}^{(\mathrm{s})} = \frac{1}{\sqrt{2}}(T_y\sigma_x + T_x\sigma_y), \tag{A41}$$

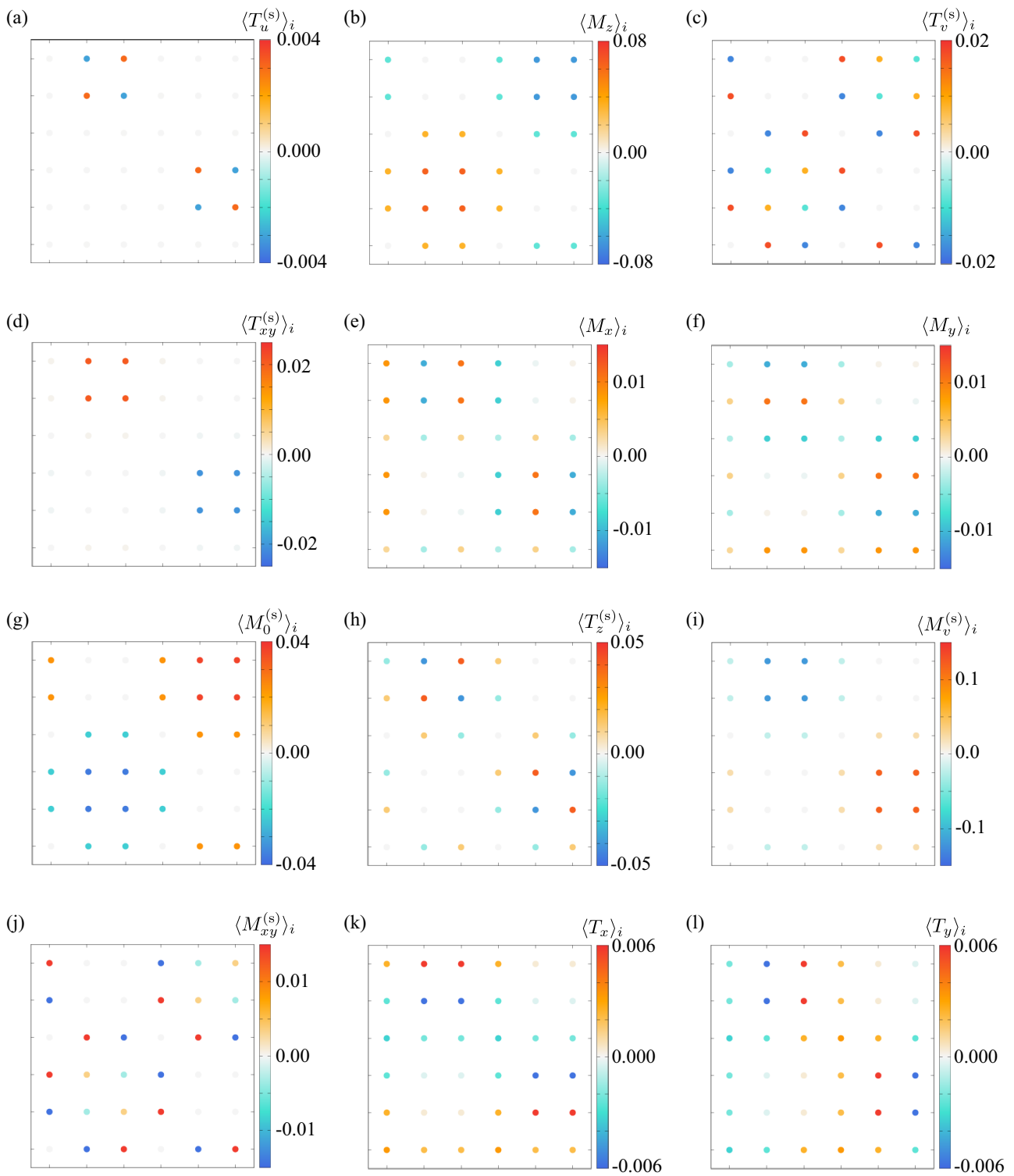where $Q_u^{(\pm)} = Q_u \pm \sqrt{3}Q_v$ and $Q_v^{(\pm)} = \pm\sqrt{3}Q_u + Q_v$.

Appendix B. Real-Space Multipole Configurations

Below, we show the real-space multipole configurations of the Néel-type vortex crystal and the Néel-type skyrmion crystal. Figures A1 and A2 show the electric-type and magnetic-type multipole configurations of the Néel-type vortex crystal in real space, which correspond to Figure 3 and Figure 4, respectively. Similarly, the electric-type and magnetic-type multipole configurations of the Néel-type skyrmion crystal in real space are shown in Figures A3 and A4, which correspond to Figure 5 and Figure 6, respectively.
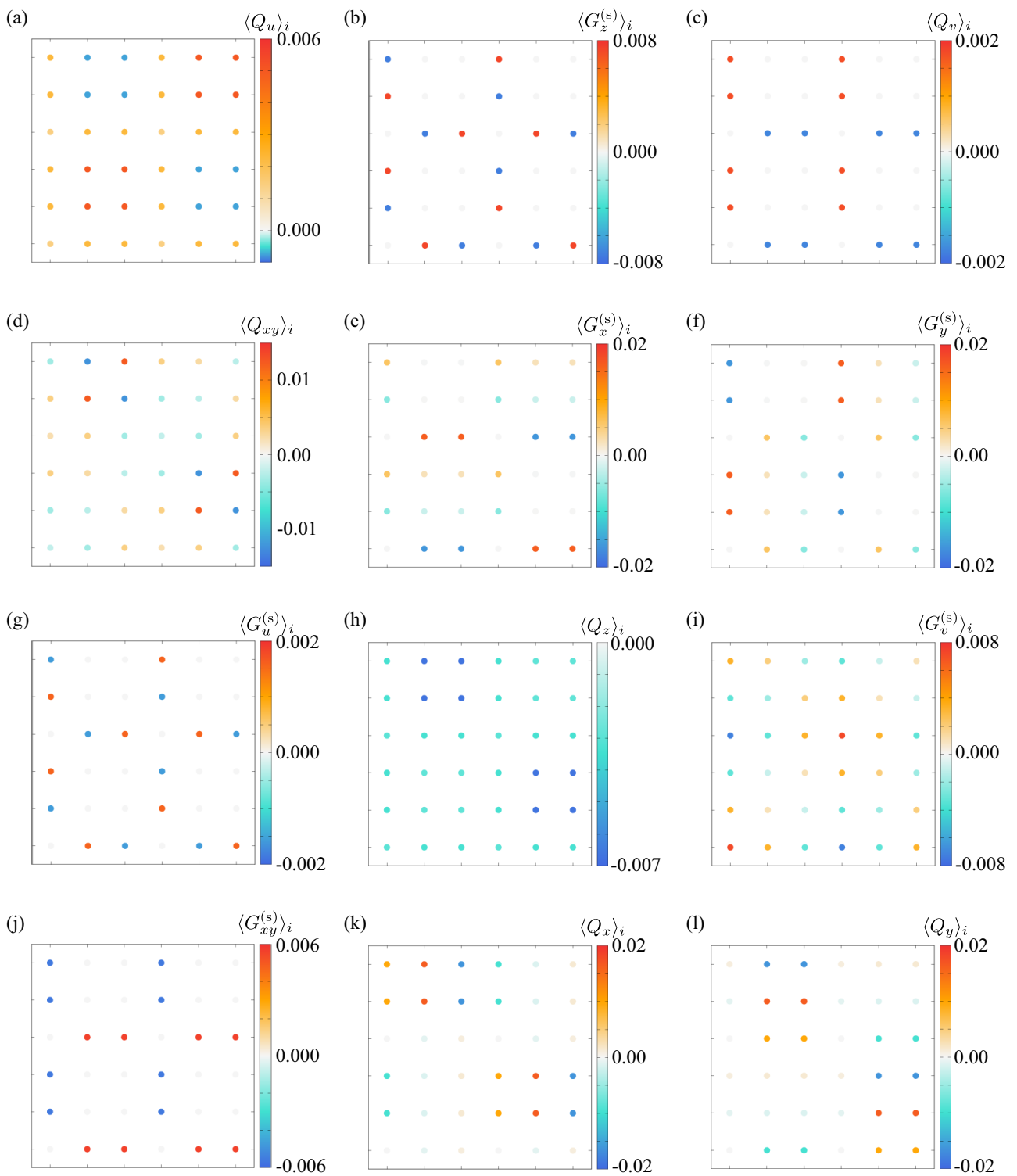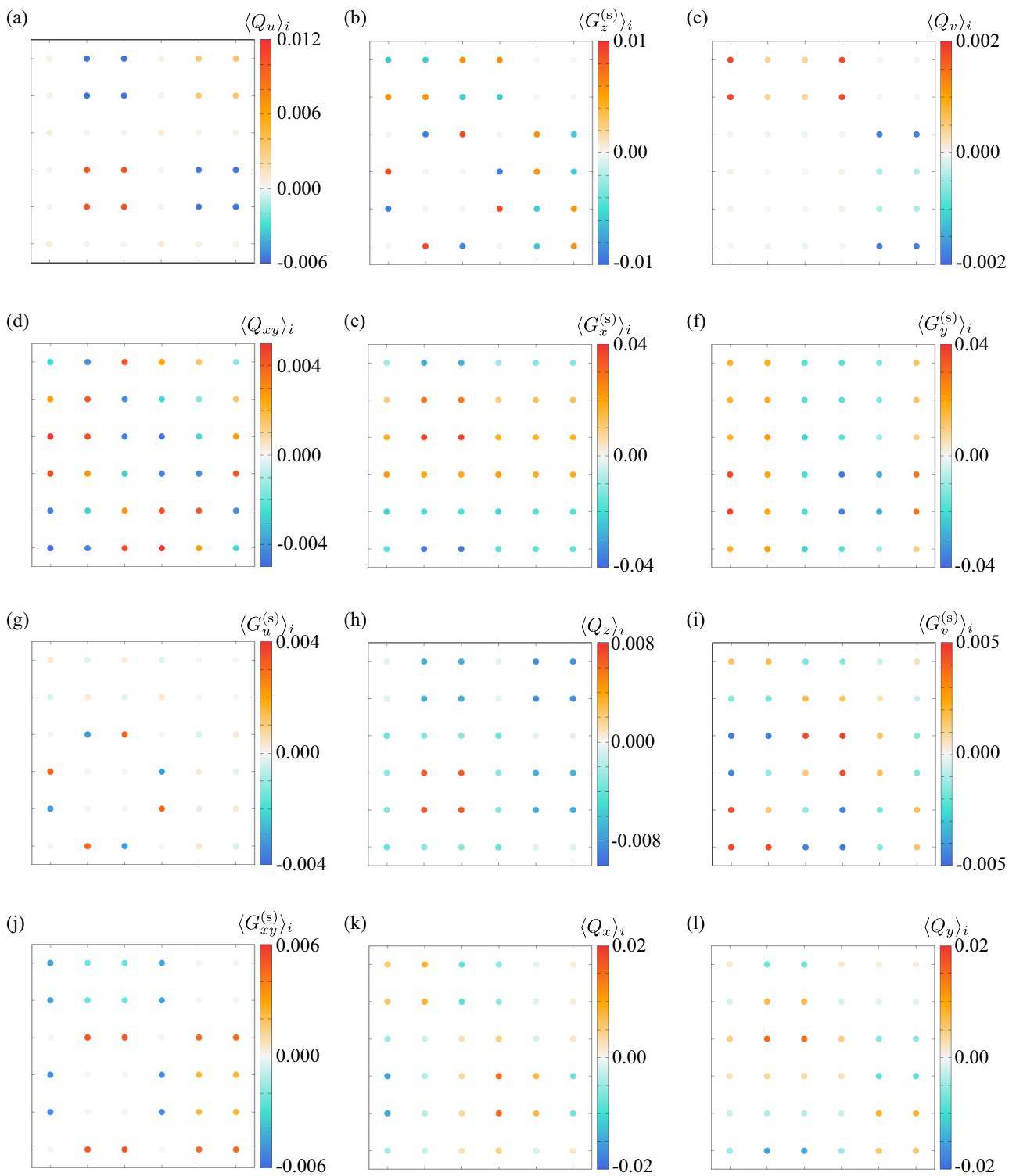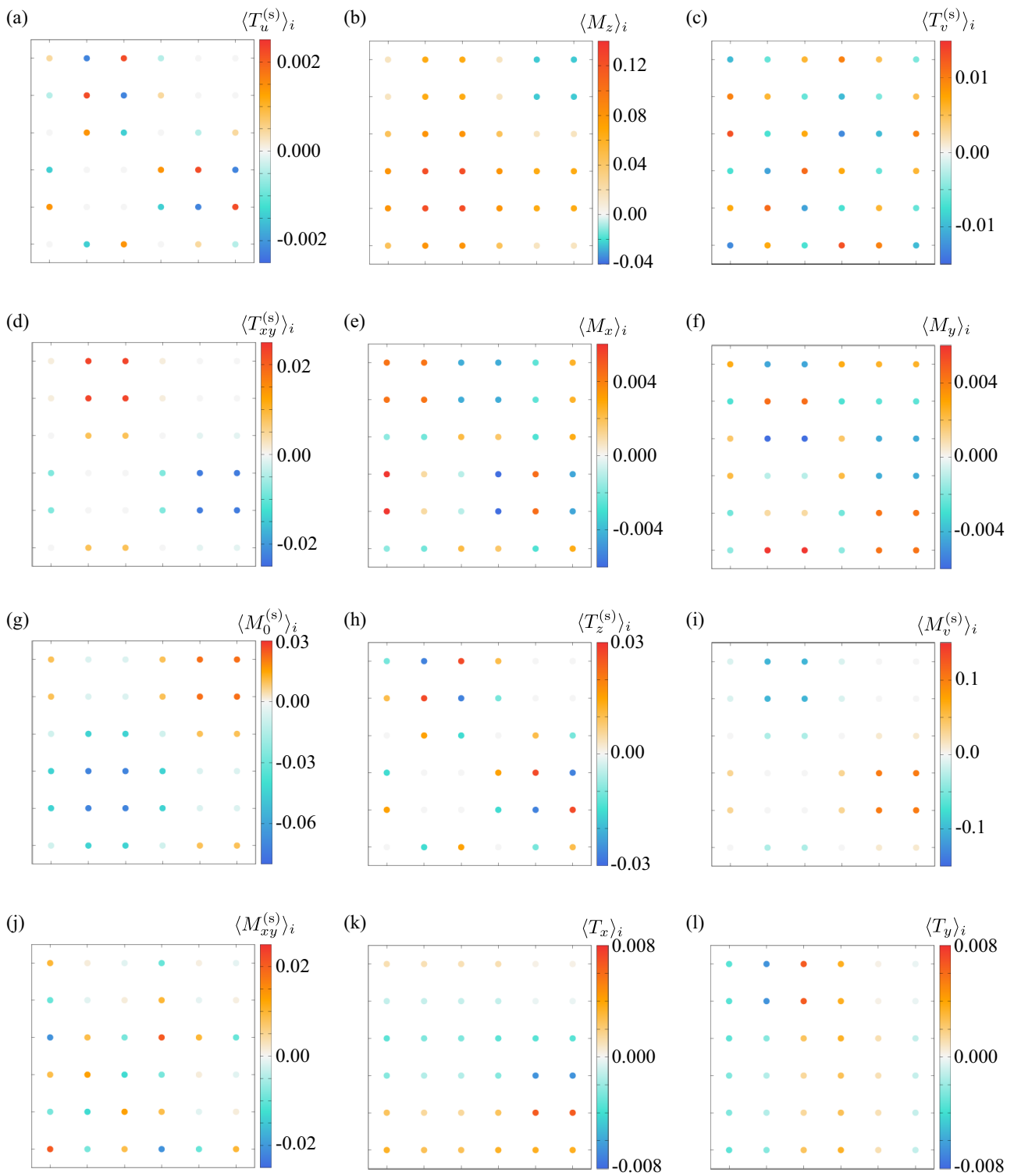
Figure A1. The real-space electric-type multipole configurations in the Néel-type vortex crystal for (**a**) $\langle Q_u \rangle$, (**b**) $\langle G_z^{(\mathrm{s})} \rangle$, (**c**) $\langle Q_v \rangle$, (**d**) $\langle Q_{xy} \rangle$, (**e**) $\langle G_x^{(\mathrm{s})} \rangle$, (**f**) $\langle G_y^{(\mathrm{s})} \rangle$, (**g**) $\langle G_u^{(\mathrm{s})} \rangle$, (**h**) $\langle Q_z \rangle$, (**i**) $\langle G_v^{(\mathrm{s})} \rangle$, (**j**) $\langle G_{xy}^{(\mathrm{s})} \rangle$, (**k**) $\langle Q_x \rangle$, and (**l**) $\langle Q_y \rangle$.

Figure A2. The real-space magnetic-type multipole configurations in the Néel-type vortex crystal for (**a**) $\langle T_u^{(\mathrm{s})} \rangle_i$, (**b**) $\langle M_z \rangle_i$, (**c**) $\langle T_v^{(\mathrm{s})} \rangle_i$, (**d**) $\langle T_{xy}^{(\mathrm{s})} \rangle_i$, (**e**) $\langle M_x \rangle_i$, (**f**) $\langle M_y \rangle_i$, (**g**) $\langle M_0^{(\mathrm{s})} \rangle_i$, (**h**) $\langle T_z^{(\mathrm{s})} \rangle_i$, (**i**) $\langle M_v^{(\mathrm{s})} \rangle_i$, (**j**) $\langle M_{xy}^{(\mathrm{s})} \rangle_i$, (**k**) $\langle T_x \rangle_i$, and (**l**) $\langle T_y \rangle_i$.

Figure A3. The real-space electric-type multipole configurations in the Néel-type skyrmion crystal for (**a**) $\langle Q_u \rangle_i$, (**b**) $\langle G_z^{(\mathrm{s})} \rangle_i$, (**c**) $\langle Q_v \rangle_i$, (**d**) $\langle Q_{xy} \rangle_i$, (**e**) $\langle G_x^{(\mathrm{s})} \rangle_i$, (**f**) $\langle G_y^{(\mathrm{s})} \rangle_i$, (**g**) $\langle G_u^{(\mathrm{s})} \rangle_i$, (**h**) $\langle Q_z \rangle_i$, (**i**) $\langle G_v^{(\mathrm{s})} \rangle_i$, (**j**) $\langle G_{xy}^{(\mathrm{s})} \rangle_i$, (**k**) $\langle Q_x \rangle_i$, and (**l**) $\langle Q_y \rangle_i$.

Figure A4. The real-space magnetic-type multipole configurations in the Néel-type skyrmion crystal for (**a**) $\langle T_u^{(\mathrm{s})} \rangle$, (**b**) $\langle M_z \rangle$, (**c**) $\langle T_v^{(\mathrm{s})} \rangle$, (**d**) $\langle T_{xy}^{(\mathrm{s})} \rangle$, (**e**) $\langle M_x \rangle$, (**f**) $\langle M_y \rangle$, (**g**) $\langle M_0^{(\mathrm{s})} \rangle$, (**h**) $\langle T_z^{(\mathrm{s})} \rangle$, (**i**) $\langle M_v^{(\mathrm{s})} \rangle$, (**j**) $\langle M_{xy}^{(\mathrm{s})} \rangle$, (**k**) $\langle T_x \rangle$, and (**l**) $\langle T_y \rangle$.

References

1. Baibich, M.N.; Broto, J.; Fert, A.; Van Dau, F.N.; Petroff, F.; Etienne, P.; Creuzet, G.; Friederich, A.; Chazelas, J. Giant magnetoresistance of (001) Fe/(001) Cr magnetic superlattices. *Phys. Rev. Lett.* **1988**, *61*, 2472. [CrossRef] [PubMed]
2. Kusters, R.; Singleton, J.; Keen, D.; McGreevy, R.; Hayes, W. Magnetoresistance measurements on the magnetic semiconductor $Nd_{0.5}Pb_{0.5}MnO_3$. *Phys. B Condens. Matter* **1989**, *155*, 362–365. [CrossRef]
3. von Helmolt, R.; Wecker, J.; Holzapfel, B.; Schultz, L.; Samwer, K. Giant negative magnetoresistance in perovskitelike $La_{2/3}Ba_{1/3}MnO_x$ ferromagnetic films. *Phys. Rev. Lett.* **1993**, *71*, 2331. [CrossRef] [PubMed]
4. Urushibara, A.; Moritomo, Y.; Arima, T.; Asamitsu, A.; Kido, G.; Tokura, Y. Insulator-metal transition and giant magnetoresistance in $La_{1-x}Sr_xMnO_3$. *Phys. Rev. B* **1995**, *51*, 14103. [CrossRef]
5. Ramirez, A. Colossal magnetoresistance. *J. Phys. Condens. Matter* **1997**, *9*, 8171. [CrossRef]
6. Tokura, Y.; Tomioka, Y. Colossal magnetoresistive manganites. *J. Magn. Magn. Mat.* **1999**, *200*, 1–23. [CrossRef]
7. Tokura, Y. (Ed.) *Colossal Magnetoresistive Oxides*; Gordon & Breach Science Publisher: London, UK, 1999.
8. Kimura, T.; Kawamoto, S.; Yamada, I.; Azuma, M.; Takano, M.; Tokura, Y. Magnetocapacitance effect in multiferroic $BiMnO_3$. *Phys. Rev. B* **2003**, *67*, 180401. [CrossRef]
9. Katsura, H.; Nagaosa, N.; Balatsky, A.V. Spin Current and Magnetoelectric Effect in Noncollinear Magnets. *Phys. Rev. Lett.* **2005**, *95*, 057205. [CrossRef]
10. Mostovoy, M. Ferroelectricity in Spiral Magnets. *Phys. Rev. Lett.* **2006**, *96*, 067601. [CrossRef]
11. Eerenstein, W.; Mathur, N.; Scott, J.F. Multiferroic and magnetoelectric materials. *Nature* **2006**, *442*, 759–765. [CrossRef]
12. Sushkov, A.B.; Aguilar, R.V.; Park, S.; Cheong, S.W.; Drew, H.D. Electromagnons in Multiferroic YMn_2O_5 and $TbMn_2O_5$. *Phys. Rev. Lett.* **2007**, *98*, 027202. [CrossRef] [PubMed]
13. Cheong, S.W.; Mostovoy, M. Multiferroics: A magnetic twist for ferroelectricity. *Nat. Mater.* **2007**, *6*, 13–20. [CrossRef] [PubMed]
14. Scott, J. Data storage: Multiferroic memories. *Nat. Mater.* **2007**, *6*, 256–257. [CrossRef]
15. Ramesh, R.; Spaldin, N.A. Multiferroics: Progress and prospects in thin films. *Nat. Mater.* **2007**, *6*, 21. [CrossRef] [PubMed]
16. Tokura, Y.; Seki, S.; Nagaosa, N. Multiferroics of spin origin. *Rep. Prog. Phys.* **2014**, *77*, 076501. [CrossRef]
17. Ohgushi, K.; Murakami, S.; Nagaosa, N. Spin anisotropy and quantum Hall effect in the *kagomé* lattice: Chiral spin state based on a ferromagnet. *Phys. Rev. B* **2000**, *62*, R6065–R6068. [CrossRef]
18. Tatara, G.; Kawamura, H. Chirality-driven anomalous Hall effect in weak coupling regime. *J. Phys. Soc. Jpn.* **2002**, *71*, 2613–2616. [CrossRef]
19. Neubauer, A.; Pfleiderer, C.; Binz, B.; Rosch, A.; Ritz, R.; Niklowitz, P.G.; Böni, P. Topological Hall Effect in the *A* Phase of MnSi. *Phys. Rev. Lett.* **2009**, *102*, 186602. [CrossRef]
20. Kanazawa, N.; Onose, Y.; Arima, T.; Okuyama, D.; Ohoyama, K.; Wakimoto, S.; Kakurai, K.; Ishiwata, S.; Tokura, Y. Large Topological Hall Effect in a Short-Period Helimagnet MnGe. *Phys. Rev. Lett.* **2011**, *106*, 156603. [CrossRef]
21. Shiomi, Y.; Kanazawa, N.; Shibata, K.; Onose, Y.; Tokura, Y. Topological Nernst effect in a three-dimensional skyrmion-lattice phase. *Phys. Rev. B* **2013**, *88*, 064409. [CrossRef]
22. Hamamoto, K.; Ezawa, M.; Nagaosa, N. Quantized topological Hall effect in skyrmion crystal. *Phys. Rev. B* **2015**, *92*, 115417. [CrossRef]
23. Göbel, B.; Mook, A.; Henk, J.; Mertig, I. Unconventional topological Hall effect in skyrmion crystals caused by the topology of the lattice. *Phys. Rev. B* **2017**, *95*, 094413. [CrossRef]
24. Leroux, M.; Stolt, M.J.; Jin, S.; Pete, D.V.; Reichhardt, C.; Maiorov, B. Skyrmion lattice topological Hall effect near room temperature. *Sci. Rep.* **2018**, *8*, 15510. [CrossRef]
25. Nakazawa, K.; Bibes, M.; Kohno, H. Topological Hall effect from strong to weak coupling. *J. Phys. Soc. Jpn.* **2018**, *87*, 033705. [CrossRef]
26. Kurumaji, T.; Nakajima, T.; Hirschberger, M.; Kikkawa, A.; Yamasaki, Y.; Sagayama, H.; Nakao, H.; Taguchi, Y.; Arima, T.h.; Tokura, Y. Skyrmion lattice with a giant topological Hall effect in a frustrated triangular-lattice magnet. *Science* **2019**, *365*, 914–918. [CrossRef]
27. Park, H.; Heinonen, O.; Martin, I. First-principles study of magnetic states and the anomalous Hall conductivity of MNb_3S_6 (M = Co, Fe, Mn, and Ni). *Phys. Rev. Mater.* **2022**, *6*, 024201. [CrossRef]
28. Oike, H.; Ebino, T.; Koretsune, T.; Kikkawa, A.; Hirschberger, M.; Taguchi, Y.; Tokura, Y.; Kagawa, F. Topological Nernst effect emerging from real-space gauge field and thermal fluctuations in a magnetic skyrmion lattice. *Phys. Rev. B* **2022**, *106*, 214425. [CrossRef]
29. Hirsch, J.E. Spin Hall Effect. *Phys. Rev. Lett.* **1999**, *83*, 1834–1837. [CrossRef]
30. Zhang, S. Spin Hall Effect in the Presence of Spin Diffusion. *Phys. Rev. Lett.* **2000**, *85*, 393–396. [CrossRef]
31. Murakami, S.; Nagaosa, N.; Zhang, S.C. Dissipationless quantum spin current at room temperature. *Science* **2003**, *301*, 1348–1351. [CrossRef]
32. Murakami, S.; Nagaosa, N.; Zhang, S.C. Spin-Hall Insulator. *Phys. Rev. Lett.* **2004**, *93*, 156804. [CrossRef] [PubMed]
33. Sinova, J.; Culcer, D.; Niu, Q.; Sinitsyn, N.A.; Jungwirth, T.; MacDonald, A.H. Universal Intrinsic Spin Hall Effect. *Phys. Rev. Lett.* **2004**, *92*, 126603. [CrossRef] [PubMed]
34. Kane, C.L.; Mele, E.J. Quantum Spin Hall Effect in Graphene. *Phys. Rev. Lett.* **2005**, *95*, 226801. [CrossRef] [PubMed]

35. Bernevig, B.A.; Hughes, T.L.; Zhang, S.C. Quantum Spin Hall Effect and Topological Phase Transition in HgTe Quantum Wells. *Science* **2006**, *314*, 1757. [CrossRef] [PubMed]

36. Xu, C.; Moore, J.E. Stability of the quantum spin Hall effect: Effects of interactions, disorder, and Z_2 topology. *Phys. Rev. B* **2006**, *73*, 045322. [CrossRef]

37. Fujimoto, S. Emergent Nodal Excitations due to Coexistence of Superconductivity and Antiferromagnetism: Cases with and without Inversion Symmetry. *J. Phys. Soc. Jpn.* **2006**, *75*, 083704. [CrossRef]

38. Bernevig, B.A.; Zhang, S.C. Quantum Spin Hall Effect. *Phys. Rev. Lett.* **2006**, *96*, 106802. [CrossRef]

39. Sinova, J.; Valenzuela, S.O.; Wunderlich, J.; Back, C.H.; Jungwirth, T. Spin Hall effects. *Rev. Mod. Phys.* **2015**, *87*, 1213. [CrossRef]

40. Hayami, S.; Yatsushiro, M.; Kusunose, H. Nonlinear spin Hall effect in $\mathcal{PT}$-symmetric collinear magnets. *Phys. Rev. B* **2022**, *106*, 024405. [CrossRef]

41. Edelstein, V.M. Spin polarization of conduction electrons induced by electric current in two-dimensional asymmetric electron systems. *Solid State Commun.* **1990**, *73*, 233–235. [CrossRef]

42. Yip, S.K. Two-dimensional superconductivity with strong spin-orbit interaction. *Phys. Rev. B* **2002**, *65*, 144508. [CrossRef]

43. Fujimoto, S. Magnetoelectric effects in heavy-fermion superconductors without inversion symmetry. *Phys. Rev. B* **2005**, *72*, 024515. [CrossRef]

44. Shen, K.; Vignale, G.; Raimondi, R. Microscopic Theory of the Inverse Edelstein Effect. *Phys. Rev. Lett.* **2014**, *112*, 096601. [CrossRef]

45. Song, Q.; Zhang, H.; Su, T.; Yuan, W.; Chen, Y.; Xing, W.; Shi, J.; Sun, J.; Han, W. Observation of inverse Edelstein effect in Rashba-split 2DEG between $SrTiO_3$ and $LaAlO_3$ at room temperature. *Sci. Adv.* **2017**, *3*, e1602312. [CrossRef] [PubMed]

46. Yoda, T.; Yokoyama, T.; Murakami, S. Orbital Edelstein Effect as a Condensed-Matter Analog of Solenoids. *Nano Lett.* **2018**, *18*, 916–920. [CrossRef]

47. Zhou, C.; Liu, Y.P.; Wang, Z.; Ma, S.J.; Jia, M.W.; Wu, R.Q.; Zhou, L.; Zhang, W.; Liu, M.K.; Wu, Y.Z.; et al. Broadband Terahertz Generation via the Interface Inverse Rashba-Edelstein Effect. *Phys. Rev. Lett.* **2018**, *121*, 086801. [CrossRef]

48. Massarelli, G.; Wu, B.; Paramekanti, A. Orbital Edelstein effect from density-wave order. *Phys. Rev. B* **2019**, *100*, 075136. [CrossRef]

49. Xu, H.; Zhou, J.; Wang, H.; Li, J. Light-induced static magnetization: Nonlinear Edelstein effect. *Phys. Rev. B* **2021**, *103*, 205417. [CrossRef]

50. Bauer, E.; Sigrist, M. (Eds.) *Non-Centrosymmetric Superconductors: Introduction and Overview (Lecture Notes in Physics)*, 2012 ed.; Springer: Berlin/Heidelberg, Germany, 2012.

51. Yip, S. Noncentrosymmetric superconductors. *Annu. Rev. Condens. Matter Phys.* **2014**, *5*, 15–33. [CrossRef]

52. Sigrist, M.; Agterberg, D.F.; Fischer, M.H.; Goryo, J.; Loder, F.; Rhim, S.H.; Maruyama, D.; Yanase, Y.; Yoshida, T.; Youn, S.J. Superconductors with staggered non-centrosymmetricity. *J. Phys. Soc. Jpn.* **2014**, *83*, 061014. [CrossRef]

53. Yuan, N.F.Q.; Mak, K.F.; Law, K.T. Possible Topological Superconducting Phases of MoS_2. *Phys. Rev. Lett.* **2014**, *113*, 097001. [CrossRef] [PubMed]

54. Singh, R.P.; Hillier, A.D.; Mazidian, B.; Quintanilla, J.; Annett, J.F.; Paul, D.M.; Balakrishnan, G.; Lees, M.R. Detection of Time-Reversal Symmetry Breaking in the Noncentrosymmetric Superconductor Re_6Zr Using Muon-Spin Spectroscopy. *Phys. Rev. Lett.* **2014**, *112*, 107002. [CrossRef] [PubMed]

55. Ali, M.N.; Gibson, Q.D.; Klimczuk, T.; Cava, R.J. Noncentrosymmetric superconductor with a bulk three-dimensional Dirac cone gapped by strong spin-orbit coupling. *Phys. Rev. B* **2014**, *89*, 020505. [CrossRef]

56. Barker, J.A.T.; Singh, D.; Thamizhavel, A.; Hillier, A.D.; Lees, M.R.; Balakrishnan, G.; Paul, D.M.; Singh, R.P. Unconventional Superconductivity in La_7Ir_3 Revealed by Muon Spin Relaxation: Introducing a New Family of Noncentrosymmetric Superconductor That Breaks Time-Reversal Symmetry. *Phys. Rev. Lett.* **2015**, *115*, 267001. [CrossRef] [PubMed]

57. Kusunose, H.; Hayami, S. Generalization of microscopic multipoles and cross-correlated phenomena by their orderings. *J. Phys. Condens. Matter* **2022**, *34*, 464002. [CrossRef]

58. Hayami, S.; Kusunose, H. Unified description of electronic orderings and cross correlations by complete multipole representation. *J. Phys. Soc. Jpn.* **2024**, *93*, 072001. [CrossRef]

59. Kishine, J.i.; Kusunose, H.; Yamamoto, H.M. On the definition of chirality and enantioselective fields. *Isr. J. Chem.* **2022**, *62*, e202200049. [CrossRef]

60. Hayami, S.; Kusunose, H. Chiral charge as hidden order parameter in URu_2Si_2. *J. Phys. Soc. Jpn.* **2023**, *92*, 113704. [CrossRef]

61. Inda, A.; Oiwa, R.; Hayami, S.; Yamamoto, H.M.; Kusunose, H. Quantification of chirality based on electric toroidal monopole. *J. Chem. Phys.* **2024**, *160*, 184117. [CrossRef]

62. Hlinka, J. Eight Types of Symmetrically Distinct Vectorlike Physical Quantities. *Phys. Rev. Lett.* **2014**, *113*, 165502. [CrossRef]

63. Hlinka, J.; Privratska, J.; Ondrejkovic, P.; Janovec, V. Symmetry Guide to Ferroaxial Transitions. *Phys. Rev. Lett.* **2016**, *116*, 177602. [CrossRef] [PubMed]

64. Jin, W.; Drueke, E.; Li, S.; Admasu, A.; Owen, R.; Day, M.; Sun, K.; Cheong, S.W.; Zhao, L. Observation of a ferro-rotational order coupled with second-order nonlinear optical fields. *Nat. Phys.* **2020**, *16*, 42–46. [CrossRef]

65. Hayashida, T.; Uemura, Y.; Kimura, K.; Matsuoka, S.; Morikawa, D.; Hirose, S.; Tsuda, K.; Hasegawa, T.; Kimura, T. Visualization of ferroaxial domains in an order-disorder type ferroaxial crystal. *Nat. Commun.* **2020**, *11*, 4582. [CrossRef] [PubMed]

66. Hayashida, T.; Uemura, Y.; Kimura, K.; Matsuoka, S.; Hagihala, M.; Hirose, S.; Morioka, H.; Hasegawa, T.; Kimura, T. Phase transition and domain formation in ferroaxial crystals. *Phys. Rev. Materials* **2021**, *5*, 124409. [CrossRef]

67. Cheong, S.W.; Huang, F.T.; Kim, M. Linking emergent phenomena and broken symmetries through one-dimensional objects and their dot/cross products. *Rep. Prog. Phys.* **2022**, *85*, 124501. [CrossRef]

68. Hayami, S.; Oiwa, R.; Kusunose, H. Electric Ferro-Axial Moment as Nanometric Rotator and Source of Longitudinal Spin Current. *J. Phys. Soc. Jpn.* **2022**, *91*, 113702. [CrossRef]

69. Nagai, T.; Kimura, T. Chemical Switching of Ferroaxial and Nonferroaxial Structures Based on Second-Order Jahn–Teller Activity in $(Na,K)_2Hf(BO_3)_2$. *Chem. Mater.* **2023**, *35*, 4109–4115. [CrossRef]

70. Hayami, S.; Yatsushiro, M. Nonlinear nonreciprocal transport in antiferromagnets free from spin-orbit coupling. *Phys. Rev. B* **2022**, *106*, 014420. [CrossRef]

71. Yatsushiro, M.; Kusunose, H.; Hayami, S. Multipole classification in 122 magnetic point groups for unified understanding of multiferroic responses and transport phenomena. *Phys. Rev. B* **2021**, *104*, 054412. [CrossRef]

72. Bak, P.; Lebech, B. "Triple-$\vec{q}$" Modulated Magnetic Structure and Critical Behavior of Neodymium. *Phys. Rev. Lett.* **1978**, *40*, 800–803. [CrossRef]

73. McEwen, K.A.; Walker, M.B. Free-energy analysis of the single-q and double-q magnetic structures of neodymium. *Phys. Rev. B* **1986**, *34*, 1781–1783. [CrossRef] [PubMed]

74. Zochowski, S.; McEwen, K. Thermal expansion study of the magnetic phase diagram of neodymium. *J. Magn. Magn. Mater.* **1986**, *54*, 515–516. [CrossRef]

75. Forgan, E.; Rainford, B.; Lee, S.; Abell, J.; Bi, Y. The magnetic structure of $CeAl_2$ is a non-chiral spiral. *J. Phys. Condens. Matter* **1990**, *2*, 10211. [CrossRef]

76. Longfield, M.J.; Paixão, J.A.; Bernhoeft, N.; Lander, G.H. Resonant x-ray scattering from multi-k magnetic structures. *Phys. Rev. B* **2002**, *66*, 054417. [CrossRef]

77. Bernhoeft, N.; Paixão, J.A.; Detlefs, C.; Wilkins, S.B.; Javorský, P.; Blackburn, E.; Lander, G.H. Resonant x-ray scattering from $UAs_{0.8}Se_{0.2}$: Multi-*k* configurations. *Phys. Rev. B* **2004**, *69*, 174415. [CrossRef]

78. Rößler, U.K.; Bogdanov, A.N.; Pfleiderer, C. Spontaneous skyrmion ground states in magnetic metals. *Nature* **2006**, *442*, 797–801. [CrossRef] [PubMed]

79. Mühlbauer, S.; Binz, B.; Jonietz, F.; Pfleiderer, C.; Rosch, A.; Neubauer, A.; Georgii, R.; Böni, P. Skyrmion lattice in a chiral magnet. *Science* **2009**, *323*, 915–919. [CrossRef]

80. Yu, X.Z.; Onose, Y.; Kanazawa, N.; Park, J.H.; Han, J.H.; Matsui, Y.; Nagaosa, N.; Tokura, Y. Real-space observation of a two-dimensional skyrmion crystal. *Nature* **2010**, *465*, 901–904. [CrossRef]

81. Yi, S.D.; Onoda, S.; Nagaosa, N.; Han, J.H. Skyrmions and anomalous Hall effect in a Dzyaloshinskii-Moriya spiral magnet. *Phys. Rev. B* **2009**, *80*, 054416. [CrossRef]

82. Binz, B.; Vishwanath, A.; Aji, V. Theory of the Helical Spin Crystal: A Candidate for the Partially Ordered State of MnSi. *Phys. Rev. Lett.* **2006**, *96*, 207202. [CrossRef]

83. Binz, B.; Vishwanath, A. Theory of helical spin crystals: Phases, textures, and properties. *Phys. Rev. B* **2006**, *74*, 214408. [CrossRef]

84. Nagaosa, N.; Tokura, Y. Topological properties and dynamics of magnetic skyrmions. *Nat. Nanotechnol.* **2013**, *8*, 899–911. [CrossRef] [PubMed]

85. Tokura, Y.; Kanazawa, N. Magnetic Skyrmion Materials. *Chem. Rev.* **2021**, *121*, 2857. [CrossRef]

86. Kusunose, H.; Oiwa, R.; Hayami, S. Complete Multipole Basis Set for Single-Centered Electron Systems. *J. Phys. Soc. Jpn.* **2020**, *89*, 104704. [CrossRef]

87. Hayami, S.; Yambe, R. Locking of skyrmion cores on a centrosymmetric discrete lattice: Onsite versus offsite. *Phys. Rev. Res.* **2021**, *3*, 043158. [CrossRef]

88. Dzyaloshinsky, I. A thermodynamic theory of "weak" ferromagnetism of antiferromagnetics. *J. Phys. Chem. Solids* **1958**, *4*, 241–255. [CrossRef]

89. Moriya, T. Anisotropic superexchange interaction and weak ferromagnetism. *Phys. Rev.* **1960**, *120*, 91. [CrossRef]

90. Hayami, S.; Motome, Y. Néel- and Bloch-Type Magnetic Vortices in Rashba Metals. *Phys. Rev. Lett.* **2018**, *121*, 137202. [CrossRef] [PubMed]

91. Utesov, O.I. Thermodynamically stable skyrmion lattice in a tetragonal frustrated antiferromagnet with dipolar interaction. *Phys. Rev. B* **2021**, *103*, 064414. [CrossRef]

92. Hayami, S. Multiple skyrmion crystal phases by itinerant frustration in centrosymmetric tetragonal magnets. *J. Phys. Soc. Jpn.* **2022**, *91*, 023705. [CrossRef]

93. Okubo, T.; Chung, S.; Kawamura, H. Multiple-q States and the Skyrmion Lattice of the Triangular-Lattice Heisenberg Antiferromagnet under Magnetic Fields. *Phys. Rev. Lett.* **2012**, *108*, 017206. [CrossRef] [PubMed]

94. Hayami, S.; Yambe, R. Degeneracy Lifting of Néel, Bloch, and Anti-Skyrmion Crystals in Centrosymmetric Tetragonal Systems. *J. Phys. Soc. Jpn.* **2020**, *89*, 103702. [CrossRef]

95. Hayami, S.; Yambe, R. Helicity locking of a square skyrmion crystal in a centrosymmetric lattice system without vertical mirror symmetry. *Phys. Rev. B* **2022**, *105*, 104428. [CrossRef]

96. Tokunaga, Y.; Yu, X.; White, J.; Rønnow, H.M.; Morikawa, D.; Taguchi, Y.; Tokura, Y. A new class of chiral materials hosting magnetic skyrmions beyond room temperature. *Nat. Commun.* **2015**, *6*, 7638. [CrossRef]

97. Karube, K.; White, J.; Reynolds, N.; Gavilano, J.; Oike, H.; Kikkawa, A.; Kagawa, F.; Tokunaga, Y.; Rønnow, H.M.; Tokura, Y.; et al. Robust metastable skyrmions and their triangular–square lattice structural transition in a high-temperature chiral magnet. *Nat. Mater.* **2016**, *15*, 1237. [CrossRef]

98. Karube, K.; White, J.S.; Morikawa, D.; Dewhurst, C.D.; Cubitt, R.; Kikkawa, A.; Yu, X.; Tokunaga, Y.; Arima, T.H.; Rønnow, H.M.; et al. Disordered skyrmion phase stabilized by magnetic frustration in a chiral magnet. *Sci. Adv.* **2018**, *4*, eaar7043. [CrossRef]

99. Karube, K.; White, J.S.; Ukleev, V.; Dewhurst, C.D.; Cubitt, R.; Kikkawa, A.; Tokunaga, Y.; Rønnow, H.M.; Tokura, Y.; Taguchi, Y. Metastable skyrmion lattices governed by magnetic disorder and anisotropy in β-Mn-type chiral magnets. *Phys. Rev. B* **2020**, *102*, 064408. [CrossRef]

100. Henderson, M.E.; Bleuel, M.; Beare, J.; Cory, D.G.; Heacock, B.; Huber, M.G.; Luke, G.M.; Pula, M.; Sarenac, D.; Sharma, S.; et al. Skyrmion alignment and pinning effects in the disordered multiphase skyrmion material $Co_8Zn_8Mn_4$. *Phys. Rev. B* **2022**, *106*, 094435. [CrossRef]

101. Chacon, A.; Heinen, L.; Halder, M.; Bauer, A.; Simeth, W.; Mühlbauer, S.; Berger, H.; Garst, M.; Rosch, A.; Pfleiderer, C. Observation of two independent skyrmion phases in a chiral magnetic material. *Nat. Phys.* **2018**, *14*, 936–941. [CrossRef]

102. Takagi, R.; Yamasaki, Y.; Yokouchi, T.; Ukleev, V.; Yokoyama, Y.; Nakao, H.; Arima, T.; Tokura, Y.; Seki, S. Particle-size dependent structural transformation of skyrmion lattice. *Nat. Commun.* **2020**, *11*, 5685. [CrossRef]

103. Khanh, N.D.; Nakajima, T.; Yu, X.; Gao, S.; Shibata, K.; Hirschberger, M.; Yamasaki, Y.; Sagayama, H.; Nakao, H.; Peng, L.; et al. Nanometric square skyrmion lattice in a centrosymmetric tetragonal magnet. *Nat. Nanotechnol.* **2020**, *15*, 444. [CrossRef] [PubMed]

104. Khanh, N.D.; Nakajima, T.; Hayami, S.; Gao, S.; Yamasaki, Y.; Sagayama, H.; Nakao, H.; Takagi, R.; Motome, Y.; Tokura, Y.; et al. Zoology of Multiple-Q Spin Textures in a Centrosymmetric Tetragonal Magnet with Itinerant Electrons. *Adv. Sci.* **2022**, *9*, 2105452. [CrossRef] [PubMed]

105. Matsuyama, N.; Nomura, T.; Imajo, S.; Nomoto, T.; Arita, R.; Sudo, K.; Kimata, M.; Khanh, N.D.; Takagi, R.; Tokura, Y.; et al. Quantum oscillations in the centrosymmetric skyrmion-hosting magnet $GdRu_2Si_2$. *Phys. Rev. B* **2023**, *107*, 104421. [CrossRef]

106. Wood, G.D.A.; Khalyavin, D.D.; Mayoh, D.A.; Bouaziz, J.; Hall, A.E.; Holt, S.J.R.; Orlandi, F.; Manuel, P.; Blügel, S.; Staunton, J.B.; et al. Double-Q ground state with topological charge stripes in the centrosymmetric skyrmion candidate $GdRu_2Si_2$. *Phys. Rev. B* **2023**, *107*, L180402. [CrossRef]

107. Eremeev, S.; Glazkova, D.; Poelchen, G.; Kraiker, A.; Ali, K.; Tarasov, A.V.; Schulz, S.; Kliemt, K.; Chulkov, E.V.; Stolyarov, V.; et al. Insight into the electronic structure of the centrosymmetric skyrmion magnet $GdRu_2Si_2$. *Nanoscale Adv.* **2023**, *5*, 6678–6687. [CrossRef]

108. Rashba, E.I. Properties of semiconductors with an extremum loop. 1. Cyclotron and combinational resonance in a magnetic field perpendicular to the plane of the loop. *Sov. Phys. Solid State* **1960**, *2*, 1109–1122.

109. Ishizaka, K.; Bahramy, M.; Murakawa, H.; Sakano, M.; Shimojima, T.; Sonobe, T.; Koizumi, K.; Shin, S.; Miyahara, H.; Kimura, A.; et al. Giant Rashba-type spin splitting in bulk BiTeI. *Nat. Mater.* **2011**, *10*, 521–526. [CrossRef]

110. Bahramy, M.S.; Arita, R.; Nagaosa, N. Origin of giant bulk Rashba splitting: Application to BiTeI. *Phys. Rev. B* **2011**, *84*, 041202(R). [CrossRef]

111. Sunko, V.; Rosner, H.; Kushwaha, P.; Khim, S.; Mazzola, F.; Bawden, L.; Clark, O.; Riley, J.; Kasinathan, D.; Haverkort, M.; et al. Maximal Rashba-like spin splitting via kinetic-energy-coupled inversion-symmetry breaking. *Nature* **2017**, *549*, 492–496. [CrossRef]

112. Hayami, S.; Motome, Y. Charge density waves in multiple-Q spin states. *Phys. Rev. B* **2021**, *104*, 144404. [CrossRef]

113. Hayami, S.; Yanagi, Y.; Kusunose, H.; Motome, Y. Electric Toroidal Quadrupoles in the Spin-Orbit-Coupled Metal $Cd_2Re_2O_7$. *Phys. Rev. Lett.* **2019**, *122*, 147602. [CrossRef] [PubMed]